

SPECTRAL ENERGY DISTRIBUTIONS OF SEYFERT NUCLEI^a

^aBASED ON OBSERVATIONS WITH THE NASA/ESA HUBBLE SPACE TELESCOPE, OBTAINED AT THE SPACE TELESCOPE SCIENCE INSTITUTE, WHICH IS OPERATED BY THE ASSOCIATION OF UNIVERSITIES FOR RESEARCH IN ASTRONOMY, INC. UNDER NASA CONTRACT NO. NAS5-26555

ALMUDENA ALONSO-HERRERO²

Steward Observatory, The University of Arizona, 933 N. Cherry Ave., Tucson, AZ 85721

E-mail: aalonso@as.arizona.edu

ALICE C. QUILLEN²

Department of Physics and Astronomy, University of Rochester, Rochester, NY 14627

GEORGE H. RIEKE

Steward Observatory, The University of Arizona, 933 N. Cherry Ave., Tucson, AZ 85721

VALENTIN D. IVANOV²

European Southern Observatory, Ave. Alonso de Córdova No. 3107, Santiago 19001, Chile

AND

ANDREAS EFSTATHIOU

Department of Computer Science and Engineering, Cyprus College, 6 Diogenes street, 1516 Nicosia, Cyprus

Draft version October 27, 2018

ABSTRACT

We present nuclear spectral energy distributions (SEDs) in the range $0.4 - 16 \mu\text{m}$ for an expanded CfA sample of Seyfert galaxies. The spectral indices ($f_\nu \propto \nu^{-\alpha_{\text{IR}}}$) from $1 - 16 \mu\text{m}$ range from $\alpha_{\text{IR}} \sim 0.9$ to 3.8 . The shapes of the spectra are correlated with Seyfert type in the sense that steeper nuclear SEDs (νf_ν increasing with increasing wavelength) tend to be found in Seyfert 2s and flatter SEDs ($\nu f_\nu \simeq \text{constant}$) in Seyfert 1 – 1.5s. The galaxies optically classified as Seyferts 1.8s and 1.9s display values of α_{IR} as in type 1 objects, or values intermediate between those of Seyfert 1s and Seyfert 2s. The intermediate SEDs of many Seyfert 1.8 – 1.9s may be consistent with the presence of a pure Seyfert 1 viewed through a moderate amount ($A_V \lesssim 5 \text{ mag}$) of foreground galaxy extinction. We find, however, that between 10 and 20% of galaxies with broad optical line components have steep infrared SEDs.

Torus models usually adopt high equatorial opacities to reproduce the infrared properties of Seyfert 1s and 2s, resulting in a dichotomy of infrared SEDs (flat for type 1s, and steep for type 2s). Such a dichotomy, however, is not observed in our sample. The wide range of spectral indices observed in the type 2 objects, the lack of extremely steep SEDs, and the large numbers of objects with intermediate spectral indices cannot be reconciled with predictions from existing optically thick torus models. We discuss possible modifications to improve torus models, including low optical depth tori, clumpy dusty tori, and high-optical-depth tori with an extended optically thin component.

Subject headings: Galaxies: active — Galaxies: nuclei — Galaxies: photometry — galaxies: Seyfert — infrared: galaxies

1. INTRODUCTION

The discovery that Seyfert 2 galaxies such as NGC 1068 can have reflected or polarized broad-line emission has led to a ‘unified’ model in which apparent differences in the properties of active galactic nuclei (AGNs) are interpreted in terms of viewing angle toward a similar intrinsic underlying structure (Antonucci 1993). In this unification paradigm, an optically thick circumnuclear dusty torus absorbs a significant fraction of the optical/UV/X-ray luminosity of the active nucleus and reradiates this energy at infrared wavelengths. One of the challenges of the unified model has been to reconcile the observed infrared emission with that predicted from the absorbing torus.

Important observational constraints for the torus models come from the shape of the infrared spectral energy distributions (SEDs) and the silicate feature at $9.7 \mu\text{m}$. Previ-

ous studies have shown that Seyfert galaxies are stronger radiators in the mid-infrared than most non-Seyfert galaxies (e.g., Spinoglio et al. 1995; Krabbe, Böker, & Maiolino 2001) and that their infrared continua have a range of shapes from nearly flat ($\nu f_\nu \sim \text{constant}$) to steeply raising with increasing wavelengths in the region between 1 and $10 \mu\text{m}$. Seyfert 2 galaxies generally have SEDs steeper than Seyfert 1 galaxies (e.g., Rieke 1978; Edelson, Malkan, & Rieke 1987; Ward et al. 1987; Fadda et al. 1998; Alonso-Herrero et al. 2001). Torus models predict SEDs that are strongly dependent on the orientation of the torus with respect to the line of sight of the observer, as well as on the density distribution and geometry of the dusty absorbing material (Pier & Krolik 1993; Granato & Danese 1994; Efsthathiou & Rowan-Robinson 1995; Granato, Danese, & Franceschini 1997). The emission between 1 and $10 \mu\text{m}$

²Visiting Astronomer at the Infrared Telescope Facility, which is operated by the University of Hawaii under contract from the National Aeronautics and Space Administration.

is thought to arise from hot dust (up to ~ 1000 K) (e.g., Rieke & Lebofsky 1981; Barvainis 1987) in the inner part of the torus and hence hidden from sight in edge-on systems that appear to be of type 2. To match the $9.7\,\mu\text{m}$ silicate feature, apparently often in absorption in Seyfert 2 and not present or slightly in emission in Seyfert 1 spectra (Rieke & Low 1975a; Roche et al. 1991; Clavel et al. 2000), the tori are assumed to be optically thick even to far-infrared wavelengths.

Studies of AGNs have often focused on high luminosity objects (QSOs and bright Seyfert 1s) since in these objects the active nucleus dominates the emission of the host galaxy. These studies avoid the complications of interpretation when the host galaxy emission is a significant fraction of the total (e.g., Kotilainen et al. 1992; Alonso-Herrero, Ward, & Kotilainen 1996). Because modelling of SEDs is only available for a handful of relatively high-luminosity nearby AGNs (e.g., Efstathiou, Hough, & Young 1995; Alexander et al. 1999; Ruiz et al. 2001), the torus parameters are not well constrained. The high angular resolution of the Hubble Space Telescope (*HST*) now allows us to probe the nuclei with a beam area about 30 times smaller than is typically achieved with ground-based observations at visible and near-infrared wavelengths. Imagers in the mid-infrared also provide a significant improvement in angular resolution over previous studies. Such data enable us to separate the nuclear emission from that of the surrounding galaxy with unprecedented accuracy as well as to probe for lower luminosity active nuclei. Recent imaging from the Infrared Space Observatory (*ISO*) also allows us to measure the nuclear emission in the mid-infrared with improved sensitivity compared with previous observations.

We have used these capabilities on an expanded version of the CfA sample of Seyfert galaxies. The infrared SEDs of the CfA sample have been studied by Edelson et al. (1987), Pier & Krolik (1993), Maiolino et al. (1995) and Pérez García & Rodríguez Espinosa (2001). Fadda et al. (1998) compiled data from the literature and *IRAS* to produce infrared SEDs of a heterogeneous sample of Seyfert galaxies, but they mainly focused their efforts on fitting infrared colors to their model outputs. All these works noted that the relatively large apertures used were likely to be contaminated by emission from the host galaxies, a particular problem for the Seyfert 2 galaxies. To address this concern, in this paper we present high resolution IRTF K' ($2.1\,\mu\text{m}$) and L ($3.5\,\mu\text{m}$) band imaging of the CfA Seyfert galaxies, from which we have estimated the non-stellar nuclear fluxes. We combine these fluxes with measurements of the unresolved nuclear emission from optical *HST*/WFPC1 and *HST*/WFPC2 and near-infrared *HST*/NICMOS and mid-infrared measurements made from ISOCAM images, and/or small-aperture ground-based $10\,\mu\text{m}$ measurements from the literature. This suite of data is used to compare the properties of the non-stellar SEDs with the predictions of models for dusty tori.

2. THE SAMPLE

2.1. The CfA sample

Tables 1 and 2 (see also Section 2.2) list the sample of galaxies on which this paper is based. The galaxies are

from the CfA redshift survey, which is drawn from the fraction of the sky defined either by $\delta \geq 0^\circ$ and $b \geq 40^\circ$ or $\delta \geq -2^\circ.5$ and $b \leq -30^\circ$, and $m_{\text{Zw}} \leq 14.5$. The AGNs were identified by means of optical spectroscopy, thus defining a “complete” magnitude-limited sample of 49 Seyfert galaxies (Huchra & Burg 1992). Because it is not color-selected, this sample should be relatively free of selection effects that tend to enhance the proportion of galaxies with anomalously strong emission in the color used for selection (Huchra & Burg 1992; Osterbrock & Martel 1993).

Spectroscopic classifications for the CfA survey are taken from Osterbrock & Martel (1993) and references therein. However Ho, Filippenko, & Sargent (1997) identified 5 Seyfert 2 galaxies as having lower Seyfert types than listed by Osterbrock & Martel (1993). In these cases we list in Table 1, column 2 the identification from Osterbrock & Martel (1993) on the left and that from Ho et al. (1997) on the right. Ruiz, Rieke, & Schmidt (1994) detected broad components in near-infrared lines in Mkn 334 and NGC 5252 (He I at $1.083\,\mu\text{m}$) and Mkn 533/NGC 7674 (He I and Pa β). Optical polarized broad-line components were detected by Young et al. (1996) in NGC 4388, NGC 5252 and Mkn 533. Tran (2001) has found a hidden broad line region in NGC 7682. For the Seyfert 2s in Table 1 we also indicate whether such hidden broad-line regions have been detected.

2.2. The extended CfA sample of Seyfert galaxies and its completeness

The CfA sample is usually regarded as a complete sample of optically selected Seyfert galaxies. However Maiolino & Rieke (1995) show that it is incomplete both in terms of low luminosity nuclei and edge-on galaxies. Ho & Ulvestad (2001) also discuss selection biases that may affect the completeness of CfA sample. Because of the method used to identify AGNs in the CfA sample, only Seyfert 2s having the broadest, most extended wings in the observed emission lines were included in the final sample. The distinction in the original classifications between LINERs and Seyferts is also not rigorous. According to these authors the CfA sample is likely to be complete only for relatively bright objects, and the Seyfert 2s in particular are intrinsically more luminous and more radio-powerful than is typical.

To alleviate in part the possible biases in the original CfA sample, we have defined an extended sample. It includes all the Seyfert galaxies in the original CfA sample as well as those galaxies initially classified as LINERs by Huchra & Burg (1992), but later reclassified as Seyfert galaxies by Ho et al. (1997) from high S/N optical spectra. We therefore add a total of nine galaxies (see Table 2) to the original CfA sample, thus increasing its size by $\simeq 20\%$ (a total of 58 galaxies).

Our sample is still probably weighted against low-luminosity type 2 Seyferts. Table 3 compares the fractions of type 1 (1 – 1.5) and type 2 (1.8 – 2), as classified from optical spectroscopy in a number of nearby AGN samples: 1.) the RSA sample (see Maiolino & Rieke 1995); 2.) the Palomar survey (Ho et al. 1997); and 3.) the infrared-selected $12\,\mu\text{m}$ sample (Spinoglio & Malkan 1989). Since the CfA sample shows a deficit of highly inclined galaxies (see Maiolino & Rieke 1995, and Section 5.5), in this table

we make the same comparison for galaxies with axial ratios $b/a \geq 0.6$. Galaxy inclinations are taken from Ho et al. (1997) and from the RC3 (de Vaucouleurs et al. 1991). We find that in low inclination galaxies, both the extended CfA sample and the $12\mu\text{m}$ sample have slightly smaller fractions of type 2s than the Palomar and RSA samples, although the numbers are not different at a statistically significant level. If, as claimed by Ho & Ulvestad (2001), the CfA sample only contains Seyfert 2s with relatively bright broad emission lines, then the CfA sample would be biased against low luminosity type 2 AGNs rather than against pure type 2 objects (that is, those with an equatorial or near equatorial view of the AGN). And indeed, it appears from Table 3 that the Palomar survey has the highest fraction of type 2 objects, probably because the high quality of its spectra allows detection of very low luminosity objects.

3. OBSERVATIONS

3.1. IRTF K' and L band observations

We have obtained high resolution K' ($\lambda_{\text{central}} = 2.12\mu\text{m}$) and L band ($\lambda_{\text{central}} = 3.51\mu\text{m}$) imaging of 34 CfA Seyfert galaxies using NSFCam (Rayner et al. 1993; Shure et al. 1994) at the 3.8m NASA IRTF telescope on Mauna Kea. The observations were made in August 1999, March 2000, August 2000 and May 2001. We used the $0.3''/\text{pixel}$ plate scale. The nuclei of the galaxies were sufficiently bright that we were able to use the tip-tilt capability during the first three campaigns (it was not available during the fourth campaign), thus improving the image quality. Typical integration times were 300 seconds in the K' band and 720 – 1200 seconds (depending on the galaxy brightness) in the L band. In Figure 1 we show three galaxies displaying extended emission in the L band. The spatial resolution (FWHM) in the L band as measured from the standard stars was $0.6'' - 0.9''$.

Standard data reduction procedures were applied for the K' images and for bright sources in the L band. Because of the short individual exposures in the L band (to avoid saturation), a number of galaxies were not detected on individual exposures, and thus the images had to be shifted to a common position and coadded using the nominal telescope offsets (blind offsets, see Table 4). In these cases the morphology and flux of the unresolved component cannot be determined, and only the integrated flux can be measured.

Conditions were photometric during all runs except for one night during the August 2000 campaign. Throughout the nights we obtained observations of standard stars from Elias et al. (1982) for photometric calibration. The typical rms scatter in these calibration observations is $0.04 - 0.06$ mag in both K' and L bands. The major source of uncertainty is the background subtraction, especially at the longer wavelengths (L) for the faint sources. In Table 4 we give the K' and L band aperture photometry.

3.2. Optical and near-infrared wavelengths: *HST* archival images

HST/NICMOS images of the CfA sample were taken for 22 Seyfert 1.8 – 2 galaxies with the NIC1 camera ($0.043''/\text{pixel}$) at $1.1\mu\text{m}$ (F110W filter) and $1.6\mu\text{m}$ (F160W filter) as part of proposal 7867 and are de-

scribed by Martini & Pogge (1999) and Martini et al. (2001). NGC 1068 was a guaranteed time target. In addition, some of the CfA Seyfert 1 – 1.5 galaxies were observed as part of a number of GTO and GO proposals, mainly through the NIC2 ($0.076''/\text{pixel}$) F160W filter. The F110W and F160W filters are roughly equivalent to the ground-based broadband J and H filters. Details on the *HST*/NICMOS observations, data reduction and fluxes for the CfA Seyferts can be found in Quillen et al. (2001).

When possible we also used WFPC2 archival images through the F606W filter (described by Malkan, Gorjian, & Tam 1998). If these images were saturated we used images taken through other filters or obtained the fluxes for the unresolved component from the literature (Ho & Peng 2001 for WFPC1 or WFPC2). See Tables 1 and 2 for the filters.

3.3. Mid-infrared wavelengths

Mid-infrared (6.75 and $9.63\mu\text{m}$) fluxes measured from *ISO*/ISOCAM images were taken from Clavel et al. (2000). The FWHM of the ISOCAM PSF is approximately $\sim 4 - 5''$ (Clavel et al. 2000). For a few galaxies which were not part of this program we obtained ISOCAM reduced images from the *ISO* archive. We also make use of the $16\mu\text{m}$ *ISO*/ISOPHOT fluxes measured for the CfA Seyferts by Pérez García & Rodríguez Espinosa (2001). In addition, we obtained ground-based small aperture N -band ($10.6\mu\text{m}$) fluxes from the literature, both to compare with the lower resolution ISOCAM observations, and to use for those galaxies where ISOCAM data are not available.

In Table 1 and Table 2 we summarize the available *HST*/WFPC1, WFPC2 and NICMOS, IRTF $K'L$ and *ISO* and ground-based mid-infrared observations for the CfA Seyfert galaxies, along with appropriate references when the data were taken from the literature.

4. THE UNRESOLVED EMISSION

The contribution from the underlying galaxy can dominate the central emission in Seyfert 2 galaxies, especially at wavelengths shorter than approximately $2\mu\text{m}$ (see e.g., Alonso-Herrero, Ward, & Kotilainen 1996; Alonso-Herrero et al. 2001) and can also be significant in Seyfert 1 galaxies (e.g., Kotilainen et al. 1992). It is therefore essential to eliminate the stellar contributions to isolate the non-stellar emission from the AGN. Since the data used in this work have been obtained with different instruments, the methods for obtaining the unresolved emission are slightly different, as we describe below.

4.1. *HST* images

In Quillen et al. (2001) we estimated the flux from the unresolved component in the F160W filter ($1.6\mu\text{m}$) by fitting the sum of a galaxy profile and the point spread function (PSF) for a large number of Seyfert galaxies. For the underlying galaxy the profiles were fitted by exponential and power laws convolved with the appropriate NICMOS PSF generated by Tinytim (Krist et al. 1998). Here we applied the same procedure for the NICMOS NIC1 F110W images ($1.1\mu\text{m}$) and the WFPC2 optical images. In addition we obtained nuclear WFPC1 or WFPC2 fluxes for a

number of galaxies from Peng & Ho (2001), see Tables 1 and 2. These authors fitted a two dimensional model consisting of an analytical description for the bulge light plus an additional point source for the nucleus, convolved with an appropriate synthetic PSF. Their modeling for the unresolved component is thus similar to ours.

4.2. K' and L -band images

We estimated the non-stellar fractions at K' and L band by fitting the PSF surface brightness profile to the nucleus of the galaxy, and assumed that the fitted PSF integrated flux represents the unresolved component (see Alonso-Herrero et al. 1998 for more details). The FWHMs of the PSF in the K' and L band were measured from standard star observations and from stars present in the images (only in K'). We also produced surface brightness profiles of the host galaxies to determine the amount of extended emission.

In Table 4, column (2) gives the measured FWHM of the nuclear emission in the L band, column (6) is the fraction of unresolved emission in a $3''$ -diameter aperture, and column (7) is the nuclear morphology in the L band. As can be seen from this table the fraction of unresolved emission in the L band within a $3''$ -diameter aperture varies from 16 to 100%, although in most cases is within 40 – 70%. McLeod & Rieke (1995) also obtained estimates of the unresolved fluxes in the K band. We find that our estimates agree with theirs to within the photometric and fitting errors of both works.

4.3. Mid-infrared wavelengths and contribution from star formation to ISO fluxes

In AGNs past $\simeq 3\mu\text{m}$ we expect the contribution from the underlying old stellar population to the nuclear fluxes to be much reduced compared to that at shorter wavelengths. However if the nuclear stellar population is dominated by a starburst there may be contamination at wavelengths $> 3\mu\text{m}$. We note that recently Krabbe et al. (2001) and Lira et al. (2001) have obtained ground-based N imaging of small samples of Seyfert galaxies and found that the mid-infrared $10\mu\text{m}$ emission is dominated by a central unresolved source; however, a low surface brightness extended component powered by star formation might not be apparent in such data.

Because of the relatively large $ISO/ISOCAM$ aperture (diameter of $18''$, see Clavel et al. 2000) we need to determine whether the 6.75 and $9.63\mu\text{m}$ ISO fluxes are contaminated by circumnuclear star formation. To this end we compare 6 cm radio measurements through a large ($\simeq 15''$) aperture with those through a small ($\simeq 0.3''$) aperture. The radio measurements are taken from Kukula et al. (1995) for the small aperture and from Rush, Malkan, & Edelson (1996) for the large aperture. The small aperture radio measurements of Seyfert galaxies are most likely to originate in the AGN whereas the large aperture fluxes will include contributions from both the AGN and extended star formation. Small $6\text{ cm } f_{0.3''}/f_{15''}$ ratios are therefore a warning that there may be a significant level of circumnuclear star formation within the large aperture.

In Table 5 we list Seyfert galaxies in the CfA sample with available ISO fluxes and fractions of nuclear to $15''$

radio emission of $\leq 15\%$. For comparison in this table we also list, when available, the $10\mu\text{m}$ ground-based² to ISO flux ratios, and whether there is evidence for extended emission in the L band and ISO images. The latter are from Clavel et al. (2000) and our own analysis of the images. We have also included in this table NGC 5929 and NGC 5940 as they appear to have extended mid-infrared emission from the comparison of the ISO and ground-based $10\mu\text{m}$ fluxes.

Mkn 334, Mkn 841 and NGC 4051 have small $f_{0.3''}/f_{15''}$ ratios at 6 cm , but do not appear to be extended in either the ISO or the L -band images, and have mid-infrared ground to ISO ratios consistent with most of this emission stemming from a small region. NGC 4388 shows evidence for extended radio emission, but the ISO images reveal the presence of a bright point source on top of an extended diffuse component, so it is likely that most of the ISO fluxes are unresolved emission originating in the AGN.

NGC 1144, NGC 3982, NGC 5033 and Mkn 266SW are cases where the ISO mid-infrared fluxes may contain a significant contribution from circumnuclear star formation. In NGC 1144 there are H II regions a few arcseconds SW of the nucleus (see Figure 1 and also Hippelein 1989). In NGC 3982 there are H II regions within the $18''$ ISO aperture (González-Delgado et al. 1997), whereas in NGC 5033 bright H II regions are present in the spiral arms to within $5''$ of the nucleus (Evans et al. 1996). Mkn 266SW is part of an interacting system whose nuclei are separated by $\simeq 10''$. Since we detect L -band emission from both nuclei (see Table 4) it is possible that the ISO fluxes also contain contributions from both nuclei. For these galaxies we list in Table 6 small aperture ground-based mid-infrared fluxes. If these are not available then the ISO fluxes are given as upper limits to the unresolved emission. Although there may still be some contribution from a compact starburst even for the small aperture ground-based measurements, it will be energetically less important than that from extended star formation (Imanishi 2002).

5. OBSERVED SPECTRAL ENERGY DISTRIBUTIONS

In Tables 6 and 7, columns (2) through (9), we have summarized the optical and near- and mid-infrared unresolved (non-stellar) fluxes for the CfA Seyfert 2s and Seyfert 1s, respectively. Errors in all the unresolved fluxes are on average $\pm 30\%$. We also indicate in these two tables, when appropriate, the upper limits to the nuclear fluxes. Because of the large aperture of the $ISO/ISOPHOT$ $16\mu\text{m}$ measurements, we show all the fluxes at this wavelength as upper limits as they may be contaminated to some degree by emission from the host galaxy.

In Figure 2 we present the non-stellar SEDs of NGC 1068 and NGC 4151, where the 1.1 through $2.2\mu\text{m}$ data points are from $HST/NICMOS$, and the 3.8 and $4.8\mu\text{m}$ are ground-based data, all taken from Alonso-Herrero et al. (2001) and references therein. We also show the ISO spectrum of the AGN component of NGC 1068 (Le Floc'h et al. 2001), as well as the $ISO/ISOPHOT$ $16\mu\text{m}$ data points from Pérez García & Rodríguez Espinosa (2001). The additional mid-infrared wavelength points are ground-based observations through small ($6 - 8.5''$) apertures (Rieke & Low 1972; 1975a; 1975b) and diffraction

²Typically the apertures of ground-based data were of the order of $5-8.5''$.

limited measurements of the central emission (Alloin et al. 2000 for NGC 1068 and Radomski et al. 2002 for NGC 4151). These two galaxies provide a guide to the behavior of the other galaxies in the sample, for which less complete data are available. From 10 to $34\mu\text{m}$, the SEDs are very similar, and both are flat in νf_ν . From 1 to $10\mu\text{m}$, the SED of NGC 1068 has the appearance of a very strongly reddened version of the SED of NGC 4151. Qualitatively, this difference is as predicted by the unified model.

The non-stellar optical through mid-infrared ($\simeq 16\mu\text{m}$) SEDs of the remaining galaxies are presented in Figures 3, 4 and 5 for the CfA Seyfert 1 – 1.5s, Seyfert 1.8 – 1.9s and Seyfert 2s, respectively. When plotting the SEDs and fitting the spectral indices (next section) the ground-based N -band fluxes (derived to give monochromatic fluxes of Rayleigh-Jeans spectra) need to be corrected to $\nu f_\nu = \text{constant}$ by multiplying them by a factor of 1.22 (see also Edelson et al. 1987).

Variability in the near-infrared and optical region (e.g., Clavel, Wamsteker, & Glass 1989) is a concern when assembling SEDs of AGN from multiple data sources. Most of these data were observed within a time period of a couple years: the *ISO* lifetime was Nov. 1995 through May 1998, and the NICMOS lifetime prior the cryocooler era was Feb. 1997 through Dec. 1998. Most of the WFPC2 images were observed within a year of these operational lifetimes. A number of the CfA galaxies have duplicate NICMOS observations. NGC 5273, NGC 5033, NGC 5347, UGC 12138, and UM 146 displayed variable levels (over a time scale of a few months) of the unresolved emission at $1.6\mu\text{m}$ but Mkn 573, NGC 5252 and Mkn 471 did not (Quillen et al. 2000). Typical levels of variations in the near-infrared (at $1.6\mu\text{m}$) fluxes are up to $\sim 20\%$ (Quillen et al. 2000). This level of variation should be within the uncertainties of the unresolved flux estimates in the near-infrared, so we do not expect that our SEDs are strongly affected by intrinsic variability.

A common parametrization to describe the non-stellar SEDs of AGN is to fit a spectral index (α) so that the observed fluxes can be expressed as power laws, $f_\nu \propto \nu^{-\alpha}$. For a significant fraction of the Seyfert 2s we only have upper limits to the unresolved emission – at short wavelengths if a point source was not detected, and at longer wavelengths if there is evidence for stellar emission. We use the package ASURV (La Valley, Isobe, & Feigelson 1992) to fit the SEDs because it allows us to include upper limits. We have fit spectral indices in the optical to infrared (up to $16\mu\text{m}$) spectral range ($\alpha_{\text{opt-IR}}$) and in the infrared ($1 - 16\mu\text{m}$) spectral range alone (α_{IR}). The spectral indices are presented in the last two columns of Tables 6 and 7. In Figure 6 we show the distributions of the fitted spectral indices in terms of the Seyfert type as derived from optical spectroscopy.

5.1. The effects of extended foreground extinction in the host galaxy

Before we discuss the observed SEDs of the CfA Seyferts and compare them with torus models, we must consider the effects of dust in the host galaxy. Most of the Seyfert galaxies in the CfA sample have dust near their nuclei (Martini & Pogge 1999; Pogge & Martini 2002). Generally the extinction is not strong enough to be prominent in

the NICMOS images (see Martini & Pogge 1999), which sets a limit on the total extinction that can be present on scales resolvable by *HST*. As can be seen from their color maps, the dust is generally located in front of the nucleus (see also Regan & Mulchaey 1999). We can therefore consider it as a purely foreground medium. Martini & Pogge (1999) used the $V - H$ colors of the Seyfert 2s in the CfA sample to derive moderate levels of optical extinction, up to $A_V \sim 5$ mag.

To illustrate the effects of dust in the host galaxy, we took SEDs produced by the tapered torus+cone models (see Section 6 and Table 8) from Efstathiou et al. (1995) and inferred their appearance as seen through a foreground dust screen. We consider three different viewing angles to the AGN: $\theta_v = 0^\circ$ (polar view of the AGN), $\theta_v = 30^\circ$ (intermediate view), and $\theta_v = 90^\circ$ (equatorial, through the torus, view of the AGN). The intermediate viewing angle has been chosen to coincide with the half opening angle of this particular torus model, which corresponds to the transition between type 1 and type 2 objects. For the foreground extinction we used values of $A_V = 0.4, 1$ and 5 mag, and the Rieke & Lebofsky (1985) extinction curve. The resulting spectra are shown in Figure 7. The reddened spectrum from a nearly face-on (polar view) torus (underlying Seyfert 1, $\theta_v = 0^\circ$) will look similar to the intrinsic spectrum at a viewing angle closer to a true Seyfert 2 ($\theta_v = 90^\circ$) given sufficient levels of foreground extinction ($A_V > 5$ mag). However, moderate amounts of extinction will not have a significant effect on the nuclear fluxes at wavelengths greater than approximately $2\mu\text{m}$. In addition, if a foreground screen of dust that is generally thick enough to modify the infrared SEDs has small holes, the view of the torus through these holes will dominate the flux in the near infrared and give an impression of a low level of extinction overall.

The torus models place the source of the near-infrared emission close to the broad-line region, and of a diameter of order 1 pc (compared with the size of about 0.01 pc for the BLR). This general geometry is supported by observations of near-infrared variability with timescales of order a year (e.g., Rieke & Lebofsky 1979; Lebofsky & Rieke 1980; Glass 1998 and references therein). To obscure the entire near-infrared-emitting region with a foreground cloud that nonetheless lets the broad emission lines through would take a highly contrived configuration for the obscuring cloud: a small hole aligned on the BLR with no other holes elsewhere where near-infrared light could escape in our direction. Thus, it is improbable that dust in the host galaxy could significantly modify the infrared SED and still allow broad lines to be detected in optical spectra.

5.2. Seyfert 1 – 1.5s

The most remarkable aspect of the optical to mid-infrared non-stellar SEDs for the type 1 – 1.5 galaxies (see Figure 3) is the high degree of uniformity, with a featureless continuum that is nearly flat in νf_ν , similar to that of NGC 4151. Overall, the newly derived SEDs are not dramatically different from those inferred in previous works, since the dominance of the AGN emission over the stellar emission in the nuclear regions makes detailed image deconvolution unimportant to derive true nuclear fluxes.

However if we compare our SEDs on a case-by-case basis with those in Edelson et al. (1987), it is clear that their Seyfert 1 SEDs between 1 and $16\mu\text{m}$ tend to appear bluer in νf_ν than ours. We believe the fluxes at shorter wavelengths in Edelson et al. (1987) may still contain some contribution from stellar emission (these authors used 8.5''-diameter apertures for their photometry).

The average values for the optical-infrared and infrared spectral indices of the Seyfert 1 – 1.5s (22 galaxies) are $\alpha_{\text{opt-IR}} = 1.59 \pm 0.30$ and $\alpha_{\text{IR}} = 1.48 \pm 0.30$, where we have excluded NGC 6104 and Mkn 993 (optically classified as Seyfert 1.5 – 1.8 and Seyfert 1.5 – 2, respectively) as they clearly show SEDs more compatible with those of type 2 objects. For comparison Edelson et al. (1987) found $\alpha = 1.15 \pm 0.29$ between $2.2\mu\text{m}$ and $25\mu\text{m}$ for the CfA sample, and Fadda et al. (1998) measured a median spectral index between $1\mu\text{m}$ and $20\mu\text{m}$ of $\alpha = 1.4$ for a heterogeneous sample of Seyfert 1s. The fact that the infrared spectral indices are on average bluer than the optical-infrared indices is probably due to the presence of some amount of foreground dust in Seyfert 1s.

However, two type 1 galaxies, Mkn 590 and NGC 7603, have well-measured SEDs that depart significantly from the pattern established for the other type 1 objects. The SEDs of both start to drop from the near infrared towards the visible, relative to the flat SEDs (in νf_ν) that are typical. We quantify this behavior from the nuclear fluxes measured at K' and L since they use identical observational techniques and were obtained simultaneously (hence variability is not an issue). Relative to the median $K' - L$ for the type 1 nuclei, an extinction of order $A_V = 10\text{ mag}$ is indicated for both galaxies. A similar extinction level would apply to the BLR, which would make the identification of these galaxies as type 1 very improbable. We conclude that it is implausible that the differences in the SEDs for these two galaxies compared with the other type 1 objects can be explained in terms of identical intrinsic SEDs modified by foreground extinction.

5.3. Seyferts 2s

In clear contrast with the CfA Seyfert 1 – 1.5s, the Seyfert 2s show a variety of spectral shapes (see Figure 5, and also Figure 6). All the Seyfert 2 galaxies have SEDs that rise steeply at increasing wavelengths ($\alpha_{\text{IR}} > 2.6$), qualitatively similar to the SED of NGC 1068. This behavior is roughly consistent with the unified model predictions for a Seyfert 2 nucleus, that is, a heavily obscured version of the typical Seyfert 1 SED.

The Seyfert 2 nuclei in the CfA sample have near-infrared colors and near-to-mid infrared colors in general redder than seen in the compilation by Fadda et al. (1998), but similar to the Seyfert 2s observed by Alonso-Herrero et al. (2001). One possibility is that the Seyfert 2 photometry compiled by Fadda et al. (1998) was still contaminated with light from the galaxy for the short wavelengths, as the determination of the unresolved component is usually limited by the seeing conditions when using ground-based observations (see Alonso-Herrero et al. 1996). The infrared spectral index of the median SED for a type 2 object in Fadda et al. (1998) is approximately $\alpha_{\text{IR}} = 2.2$ between 1 and $20\mu\text{m}$. However from Figures 5 and 6 it is clear that it is not appropriate to define a 'median' SED for type 2 objects, as it is precisely the variety of spectral shapes

that needs to be reproduced by the torus models, as we will discuss in Section 7.

Some of the type 2 nuclei have substantial amounts of extended foreground dust associated with their host galaxies. For instance NGC 4388 and NGC 5929 have measured NLR extinctions of $A_V \simeq 4\text{ mag}$ (see Veilleux et al. 1997 and Rhee & Larkin 2002, respectively). The effect of correcting the observed SEDs for the indicated amounts of foreground extinction is small. Foreground dust at the level seen in these galaxies can strongly affect the optical classification of the nuclear activity if it preferentially obscures the broad-line region (as proposed by Maiolino & Rieke 1995). However, this amount of dust does not seem capable of influencing the infrared SEDs sufficiently to account for the systematic differences seen between Seyfert 1 and Seyfert 2 SEDs.

5.4. Seyfert 1.8 – 1.9s

UGC 12138, NGC 3786, NGC 5033, and NGC 5273 (Figure 4) are optically classified as Seyfert 1.8 – 1.9s, but have nearly flat SEDs, similar to those of Seyfert 1 – 1.5s (see Figure 3). In fact their infrared spectral indices fall well within the values found for the CfA Seyfert 1 – 1.5s. The extinction maps of Martini & Pogge (1999), based on $V - H$ colors, show that all four of these galaxies are free of heavy, extended obscuring foreground clouds in their host galaxies.

We exclude from classification as type 1.9 those galaxies where the broad line component is only seen in the infrared, e.g., Pa β . The intermediate-class galaxies UM 146, Mkn 334, Mkn 471, NGC 4258, NGC 5252, and NGC 5674 (Figure 4), display intermediate SEDs (infrared spectral indices in the range $\alpha_{\text{IR}} \simeq 1.8 - 2.6$) that do not drop toward short wavelengths as steeply as NGC 1068. In most of these galaxies, unresolved nuclear emission is measured from optical and/or near-infrared *HST* images. In all of these cases, the $V - H$ images of Martini & Pogge (1999) suggest a possibility of extended obscuration from the host galaxy, although the bright and blue nucleus of Mkn 471 indicates that it is probably clear of the nearby clouds.

One possibility for the Sy1.8 – 1.9 intermediate SEDs is that they are those of a true Seyfert 1 galaxy seen through some foreground dust. However, an explanation of the steep infrared SEDs in terms of foreground dust is unlikely in the case of NGC 4258. We have used the same approach described under type 1 objects, estimating the extinction needed to redden a median type 1 infrared SED to agree with the $K' - L$ colors, and find for this galaxy a level equivalent to $A_V \geq 10$, making observation of any broad-line component very problematic. A similar conclusion holds for NGC 7479; its $K' - L$ is so red that the nucleus is not detected at the shorter wavelengths, but the NICMOS upper limits demonstrate that it is heavily obscured (if the intrinsic SED is Seyfert-1-like).

We therefore find four cases among the type 1 and intermediate-class Seyfert galaxies where broad line components are seen despite an infrared SED that is either intrinsically red or is heavily reddened. The conclusion that broad line components can escape from systems with such SEDs is reinforced by the detection by Ho et al. (1997) of broad wings on H α in NGC 1068, NGC 3982, and NGC 4388. For many of this total of seven objects,

under the unified model the "extinction" we see in the infrared SED is likely to be a property of the torus itself, rather than the result of a foreground obscuring cloud.

The Seyferts with intermediate SEDs are the most difficult for the disk and torus models to explain. The models are extremely sensitive to the viewing angle. Only for a very small range of orientation angles, just grazing the surface of the disk or torus, are intermediate SEDs predicted. The models would also predict that the broad emission lines would be obscured at virtually all viewing angles where the near-infrared emission region is obscured. Yet we find that 10 – 20% of the galaxies with detectable broad lines in the optical have red infrared SEDs. That is, a strict dichotomy of SEDs correlated with emission-line properties is predicted, but is not in accordance with our measurements.

5.5. Spectral indices and the inclination of the host galaxy

There appears to be a deficit of Seyfert 1 – 1.5 galaxies in edge-on galaxies (e.g., Keel 1980; Lawrence & Elvis 1982; Maiolino & Rieke 1995; Schmitt et al. 2001) in most of the optically selected samples. In particular, Maiolino & Rieke (1995) concluded that the CfA sample has a deficiency of Seyfert 1s in edge-on galaxies, caused by an extended torus (scale of a 100 pc) coplanar with the host galaxy that obscures the BLR. They predict that the spectrum of a Seyfert 1 galaxy will look Seyfert 2-like in many of these cases.

The behavior of the infrared SEDs provides an independent way to estimate whether AGNs are of type 1 or 2. Where the nuclei may be obscured by dust in the host galaxy, the SEDs are much less affected than the optical emission lines. Using the SED shapes, we can check whether the portion of intrinsically type 1 galaxies is similar in edge-on systems to the portion found in optically selected samples in face-on galaxies.

The axial ratios (b/a) for the extended CfA sample of Seyfert galaxies are taken from McLeod & Rieke (1995) and Ho et al. (1997). In Figure 8 we show the spectral indices as a function of the host galaxy inclination, b/a . The galaxies have been divided in Seyfert 1s (1 and 1.5 types) and Seyfert 2s (1.8, 1.9 and 2 types) according to their optical classification. We also mark in this figure for reference an axial ratio of $b/a = 0.6$ (or inclination of the host galaxy of $i = 53^\circ$). Maiolino & Rieke (1995) found that pure Seyfert 1 galaxies with axial ratios of $b/a < 0.6$ will be most likely classified as Seyfert 1.8 or 1.9. This result is confirmed by Figure 8.

If we use the infrared SED to divide galaxies into probable type 1 and type 2, we can see that in terms of the spectral index α_{IR} there are approximately equal numbers of type 1 ($\alpha_{\text{IR}} = 1.52 \pm 0.38$, 6 galaxies) and type 2 (5 galaxies) in the highly inclined galaxies in the extended CfA sample (Figure 8, right panel). These numbers are consistent those for the face-on members of the sample. This result confirms the suggestion by Maiolino & Rieke (1995) that Seyfert 1 nuclei hosted in highly inclined galaxies may be misclassified as type 2 objects. For example, studies based on optical spectroscopy and that ignore inclination effects will overestimate the portion of type 2 nuclei.

6. MODEL PREDICTIONS

For the following discussion, we assume the validity of a unified model, that is we assume that all Seyfert galaxies have similar dusty tori in their nuclei. We will try to find a geometry for these tori that is consistent with our observations.

The broadness of the spectrum in the 1 – 20 μm region and the nature of the 9.7 μm silicate feature (in absorption and emission) have been a challenge for the torus models. Compact torus models (Pier & Krolik 1993) often predict spectra that are not sufficiently broad (they lack emission in the near-infrared) or they emit too strongly in the 9.7 μm silicate feature for polar orientations. This issue has resulted in a suite of more extended disk models: the flared disk (Granato et al. 1997), the tapered disk (Efstathiou & Rowan-Robinson 1995), and the warped disk (Sanders et al. 1989). Excess emission in the near-infrared in NGC 1068 prompted Pier & Krolik (1993) to suggest that there was an additional clumpy dust component above the torus. This two component torus+cone model was also used by Efstathiou et al. (1995) to match the broad spectrum of NGC 1068.

To suppress the silicate emission in type 1 objects, previous models forced the torus geometry to have extremely steep inner regions so that the region directly illuminated by UV radiation could only be viewed at high inclination angles. Since the models were also driven by the belief that there was strong silicate absorption in the Seyfert 2s, the outer disks were arranged so that at high inclination angles the inner hotter regions were only viewed through colder material (e.g., Pier & Krolik 1993; Efstathiou & Rowan-Robinson 1995; Granato et al. 1997). Also Pier & Krolik (1993) models assumed high optical depths to be consistent with the high hard X-ray column densities often measured in Seyfert 2 galaxies.

Clavel et al. (2000) have used *ISO* spectroscopy (through a $24'' \times 24''$ aperture) to show that Seyfert 1 galaxies have little silicate emission, and a broad smooth infrared continuum. However, the Seyfert 2s displayed PAH emission and lower levels of continuum. In fact recent *ISO* and ground-based mid-infrared spectroscopy of a small number of nearby AGN show that the silicate absorption feature in some Seyfert 2s might be shallower than previously inferred (see e.g., Laurent et al. 2000, Imanishi & Ueno 2000 and Le Floc'h et al. 2001) because measurements of the nearby continuum were contaminated with PAH features originating in the host galaxy. The mid-infrared emission is probably slightly extended in many Seyfert 2s (Maiolino et al. 1995) across the region covered by the *ISO* spectra, so it is likely that there is some PAH contribution from the surrounding galaxy in a number of cases. The nuclear spectrum itself might contain little or no PAH emission. For example, little silicate absorption is seen in the *ISO*/SWS nuclear spectrum of NGC 1068 and the continuum is nearly featureless (Le Floc'h et al. 2000, see also our Figure 2, left panel).

In addition to the behavior of silicate feature, torus models can be constrained by the shapes of the SEDs for a complete sample of galaxies. To do so, we use the tapered disk model of Efstathiou & Rowan-Robinson (1995). In this geometry, the height of the disk increases with the radial distance, but tapers off to a constant height in the

outer part. The main parameters of the model are the half opening angle of the torus Θ_c , the equatorial UV optical depth τ_{UV} , the dust sublimation temperature T , the ratio between inner and outer radii r_1/r_2 , and the ratio between the scale height and the outer radius h/r_2 . Table 8 summarizes the parameters of the models used here. In addition to the torus models, we will also consider the composite torus+cone model used by Efstathiou et al. (1995) to fit the SED of NGC 1068. The viewing angles are defined as $\theta_v = 0^\circ$ for the polar view of the AGN, and $\theta_v = 90^\circ$ for the equatorial view of the AGN (note that in the Efstathiou & Rowan-Robinson 1995 models the authors measured the angles from the equator).

Because of their high equatorial opacities, the torus models presented here (but also those of Pier & Krolik 1993; Granato & Danese 1994; Granato et al. 1997) generally predict the following: (i) for viewing angles $\theta_v < \Theta_c$ an SED more or less flat in νf_ν depending on the model input parameters, and a direct view of the nuclear optical emission; (ii) for viewing angles $\theta_v > \Theta_c$, a steep near and mid-infrared SED becoming steeper as the viewing angle increases, with no direct view of the nucleus; (iii) an intermediate SED as well as some nuclear optical emission for only a very small range of possible viewing angles around $\theta_v \simeq \Theta_c$. A dichotomy of spectral shapes is thus predicted, and few, if any, Seyferts are expected to have an intermediate SED. This behavior is shown graphically in Figure 9 where the predicted infrared spectral index (α_{IR}) is plotted against the cosine of the viewing angle for some of the models described in Table 8.

7. COMPARISON WITH OBSERVATIONS

The observed distribution of α_{IR} (see Figure 6) in the extended CfA sample clearly lacks the dichotomy of spectral indices predicted by the models. As discussed in Section 5, all the Seyfert 1 – 1.5s and a large fraction of the Seyfert 1.8 – 1.9s show infrared spectral indices clustered near $\alpha_{IR} = 1.5 \pm 0.3$. Type 2 objects on the other hand show a variety of steeper spectral indices, unlike the model predictions. Moreover the large opacity torus models without the extended cone component predict steeper SEDs ($\alpha_{IR} > 4$) than observed in the CfA Seyferts for sufficiently large viewing angles. Below, we discuss a number of possibilities to reconcile the observed SEDs with the model predictions.

7.1. Torus models with low opacities

Figure 9 shows that even the model with an equatorial optical depth of $\tau_{UV} = 250$ mag ($A_V = 50$ mag) produces SEDs with $\alpha_{IR} > 4$ for viewing angles $\theta_v > 60^\circ$. The other torus models considered here with $\tau_{UV} > 250$ mag predict even steeper SEDs near an equatorial view of the AGN. Granato et al. (1997) and Fadda et al. (1998) used similar arguments based on the observed near and mid-infrared colors of Seyfert galaxies to favor low opacity (equatorial optical depths $A_V \simeq 10 - 30$ mag) for extended (a few hundred parsec) torus models.

Traditionally low opacity torus models have been ruled out because they tend to produce the $9.7\mu\text{m}$ silicate feature in emission for viewing angles of less than the half opening angle of the torus (that is, type 1 objects). Ground-based mid-infrared spectroscopy of Seyfert 1s did not show evidence for this feature in emission (Roche et

al. 1991). Recently, however, Clavel et al. (2000) have argued that the average *ISO* mid-infrared spectrum of a sample of Seyfert 1 galaxies displays some evidence for the presence of the silicate feature in emission. Spoon et al. (2002) on the other hand do not find evidence for this feature. Additional observations are needed to resolve this issue.

7.2. Torus models with an extended (optically thin) component

The extended conical component proposed in Efstathiou et al. (1995) was assumed to be optically thin and thus increases the continuum level around $3 - 5\mu\text{m}$, causing the infrared spectral index to be shallower even for high viewing angles (see Figure 9). Indeed, NGC 1068 shows emission by dust from the wall of the cavity, i.e., perpendicular to the axis of the torus and in an extended component (100 pc) coincident with the radio emission and ionization cone (see Bock et al. 1998). The Torus+Cone model of Efstathiou et al. (1995) seems to reproduce well the observed distribution of α_{IR} in the type 2 objects in the CfA sample, although it will be necessary to increase the opening angle of the torus to match the observed relative numbers of type 1 and type 2 objects in the CfA sample. This model also reproduces well the observed infrared spectral indices of Seyfert 1 – 1.5s.

This model still fails to solve the problem of the intermediate Seyferts, as infrared spectral indices in the range $\alpha_{IR} = 1.5 \pm 0.1 - 2.5 \pm 0.1$ are extremely unlikely to occur. This discrepancy can be solved with fine tuning of the models. For instance, a torus+cone model with a lower equatorial optical depth would make the transition of infrared spectral indices between type 1 and type 2 smoother, thus narrowing the range of 'unlikely' spectral indices. Another way of producing intermediate SEDs is having a range in the visibility of the scattering region. This could be done with a range in the h/r_2 parameter or if the scattering region is physically located at different distances from the nucleus. A more visible scattering region would produce a stronger $1 - 2\mu\text{m}$ continuum and therefore shallower SEDs. This could account for some of the intermediate Seyferts (Figure 4).

7.3. Clumpy torus models

Nenkova, Ivezić, & Elitzur (2002) have recently put forward a more realistic model for the emission by dust in AGNs following the initial suggestion by Pier & Krolik (1993) that the dust in the torus must be in clumps to protect the grains. The parameters of this clumpy torus are, apart from the usual geometry parameters of the torus, the radial distribution of clouds, the number of clouds and the optical depth of the individual clouds. In their model a cloud is heated by radiation from both the AGN and other surrounding clouds. The main result from this paper is that this model can reproduce simultaneously the broadness of the infrared SEDs and suppress the silicate feature emission with a few clouds (5 – 10) with optical depths $\tau_V > 60$.

Nenkova et al. (2002) only showed results from the limiting viewing angles of $\theta_v = 0^\circ$ and $\theta_v = 90^\circ$, but from their figure 3 we can see that the equatorial view of the AGN in that particular model produces an SED consistent

with the steepest SEDs in the CfA sample. It remains to be seen if their model could reproduce the variety of observed SEDs measured for type 2 objects in the CfA sample. One concern in their comparison with observations, although they will provide a more detailed modelling in the near future, is the small number of type-2 SEDs fitted, and the possibility that some of the examples are contaminated by stellar processes. For example, for Circinus, one of the Seyfert 2 galaxies used in their modelling, Ruiz et al. (2001) demonstrate that a dominant starburst component is present at wavelengths longer than approximately $25\ \mu\text{m}$.

7.4. Dust composition

The lack of deep silicate absorption features in Seyfert 2s and other arguments based on anomalous A_V/N_H ratios in AGNs have prompted the idea that the composition and properties of dust in AGNs may be different from those of Galactic dust (see e.g., Laor & Draine 1993; Maiolino et al. 2001; Maiolino, Marconi, & Oliva 2001).

Specifically, the dust around AGNs is proposed to have a large portion of large grains (Maiolino et al. 2001; Maiolino, Marconi, & Oliva 2001). In that case, the extinction curve would be flatter than the standard Galactic extinction curve. A model with a higher fraction of large grains (or fewer silicates) means we can have a flat type 1 spectrum (with weak or no silicate emission feature) with a lower optical depth, as well as shallower SEDs for viewing angles $\theta_v > \Theta_c$ (that is, type 2s). Fadda et al. (1998) have shown the effects on near infrared and mid infrared colors using models with fewer silicate grains than the standard Galactic dust composition. Such models would be in better agreement with our findings for the extended CfA sample.

8. SUMMARY

We define an extended CfA sample of Seyfert galaxies composed of the original CfA Seyferts and those galaxies initially classified as LINERs, but later reclassified as Seyferts from higher S/N optical spectra. For this sample, we present high resolution IRTF K' ($2.2\ \mu\text{m}$) and L -band ($3.5\ \mu\text{m}$) images and compile *HST*, *ISO* and ground-based observations in the spectral region $0.4\text{--}16\ \mu\text{m}$. These data have been used to determine the unresolved nuclear emission with improved accuracy over any previous studies.

The resulting spectral energy distributions are used to test and constrain unified models for the dusty tori in the active nuclei. We find that the fitted infrared spectral indices ($f_\nu \propto \nu^{-\alpha_{\text{IR}}}$) between 1 and $16\ \mu\text{m}$ are correlated with the Seyfert type in the sense that steeper SEDs tend to be found in Seyfert 2s and flatter ones in Seyfert 1 – 1.5s. The majority of galaxies optically classified as Seyfert types 1.8 and 1.9 display infrared spectral indices and SEDs either similar to those of type 1 objects or intermediate between Seyfert 1s and Seyfert 2s. The intermediate SEDs of many Seyfert 1.8 – 1.9s may be consistent

with the presence of a pure Seyfert 1 viewed through a moderate amount ($A_V \lesssim 5\ \text{mag}$) of foreground galaxy extinction.

However, the abrupt division in SED shape correlated with emission-line properties that would be predicted by an optically thick torus model —flat for type 1s and steep for type 2s— is not observed. Discrepancies with this model include the wide range of spectral indices observed in type 2 objects, the lack of extremely steep SEDs, and the large number of objects with intermediate properties. In addition, there are a surprisingly large number of galaxies with broad-line components and steep SEDs, a combination that conventional torus models would predict is very rare.

These results, combined with the lack of deep $9.7\ \mu\text{m}$ silicate absorption feature in Seyfert 2s and the possible presence of silicate emission in Seyfert 1s (Clavel et al. 2000), suggest that the region of infrared emission might not be as optically thick as previously considered. Although X-ray and maser observations show that high opacity material does exist near the AGN, it is not clear whether this material is responsible for the infrared emission. In a recent paper, Risaliti, Elvis, & Nicastro (2002) have shown that the observed fast variability (a few months) of hard X-ray column densities in Seyfert 2s is not consistent with the absorbing material being located in the standard parsec scale torus. Since this material may be closer to the black hole than the region responsible for the infrared emission in Seyfert galaxies, the hard X-ray column densities might not be useful for constraining the torus optical depth.

Other possible explanations for the observed SEDs include an optically thick torus with an additional optically thin infrared component (such as from a cone of dust clouds: Efstathiou et al. 1995) to account for the lack of very steep SEDs and the lack of deep silicate absorption features. Another promising approach is the clumpy torus model of Nenkova et al. (2002).

We are grateful to Emeric Le Floch for providing us with the *ISO* nuclear spectrum of NGC 1068, and to Paul Martini, Maia Nenkova and Moshe Elitzur for stimulating conversations. We also thank the IRTF staff for their support during the observing campaigns. Support for this work was provided by NASA through grant number GO-07869.01-96A from the Space Telescope Institute, which is operated by the Association of Universities for Research in Astronomy, Incorporated, under NASA contract NAS5-26555. We also acknowledge support from NASA projects NAG-53359 and NAG-53042 and from JPL Contract No. 961633.

This research has made use of the NASA/IPAC Extragalactic Database (NED) which is operated by the Jet Propulsion Laboratory, California Institute of Technology, under contract with the National Aeronautics and Space Administration.

REFERENCES

- Alexander, D. M., Efstathiou, A., Hough, J., Aitken, D., Lutz, D., Roche, P., & Sturm, E. 1999, MNRAS, 310, 78
- Alloin, D., Pantin, E., Lagage, P. O. & Granato, G. L. 2000, A&A, 363, 926
- Alonso-Herrero, A., Quillen, A. C., Simpson, C., Efstathiou, A., & Ward, M. J. 2001, AJ, 121, 1369
- Alonso-Herrero, A., Simpson, C., Ward, M. J., & Wilson, A. S. 1998, ApJ, 495, 196 288, 977

- Alonso-Herrero, A., Ward, M. J., & Kotilainen, J. K. 1996, *MNRAS*, 278, 902
- Antonucci, R. R. J. 1993, *ARA&A*, 31, 473
- Barvainis, R. 1987, *ApJ*, 320, 537
- Bendo, G. J. et al. 2002, *AJ*, 123, 3067
- Bock, J. J., Marsh, K. A., Ressler, M. E., & Werner, M. W. 1998, *ApJ*, 504, L5
- Chary, R., Becklin, E. E., Evans, A. S., Neugebauer, G., Scoville, N. Z., Matthews, K., & Ressler, M. E. 2000, *ApJ*, 531, 756
- Clavel, J., Wamsteker, W., & Glass, I. S. 1989, *ApJ*, 337, 236
- Clavel, J., Schulz, B., Altieri, B., Barr, P., Claes, P., Heras, A., Leech, K., Metcalfe, L., & Salama, A. 2000, *A&A*, 357, 839
- de Vaucouleurs, G., de Vaucouleurs, A., Corwin, J. R., Buta, R. J., Paturel, G., & Fouque, P. 1991, *Third reference catalogue of Bright galaxies*, New York, Springer-Verlag
- Devereaux, N. 1987, *ApJ*, 323, 91
- Edelson, R. A., Malkan, M. A., & Rieke, G. H. 1987, *ApJ*, 321, 233
- Efstathiou, A., Hough, J. H., & Young, S. 1995, *MNRAS*, 277, 1134
- Efstathiou, A., & Rowan-Robinson, M. 1995, *MNRAS*, 273, 649
- Elias, J. H., Frogel, J. A., Matthews, K., & Neugebauer, G. 1982, *AJ*, 87, 1029
- Ellis, R. S., Gondhalekar, P. M., & Efstathiou, G. 1982, *MNRAS*, 201, 223
- Evans, I. N., Koratkar, A. P., Storchi-Bergmann, T., Kirkpatrick, H., Heckman, T. M., & Wilson, A. S. 1996, *ApJS*, 105, 93
- Fadda, D., Giuricin, G., Granato, G. L., & Vecchies, D. 1998, *ApJ*, 496, 117
- Glass, I. S. 1998, *MNRAS*, 197, 18
- González-Delgado, R. M., Pérez, E., Tadhunter, C., Vilchez, J. M., Rodríguez-Espinoza, J. M. 1997, *ApJS*, 108, 155
- Goodrich, R. W. 1995, *ApJ*, 440, 141
- Granato, G. L., & Danese, L. 1994, *MNRAS*, 268, 235
- Granato, G. L., Danese, L., & Franceschini, A. 1997, *ApJ*, 486, 147
- Hippelein, H. H. 1989, *A&A*, 216, 11
- Ho, L. C., Filippenko, A. V., & Sargent, W. L. W. 1997, *ApJS*, 112, 315
- Ho, L. C., & Peng, C. Y. 2001, *ApJ*, 555, 650
- Ho, L. C., & Ulvestad, J. S. 2001, *ApJ*, 133, 77
- Huchra, J., & Burg, R. 1992, *ApJ*, 393, 90
- Imanishi, M. 2002, *ApJ*, 569, 44
- Imanishi, M. & Ueno, S. 2000, *ApJ*, 535, 626
- Jiménez-Benito, L., Díaz, A. I., Terlevich, R., & Terlevich, E. 2000, *MNRAS*, 317, 907
- Keel, W. C. 1980, *AJ*, 85, 198
- Kotilainen, J. K., Ward, M. J., Boisson, C., DePoy, D. L., Smith, M. G., & Bryant, L. R. 1992, *MNRAS*, 256, 125
- Krabbe, A., Böker, T., & Maiolino, R. 2001, *ApJ*, 557, 626
- Krist, J. E., Golimowski, D. A., Schroeder, D. J., & Henry, T. J. 1998, *PASP*, 110, 1046
- Kukula, M. J., Pedlar, A., Baum, S. A., & O'Dea, C. P. 1995, *MNRAS*, 276, 1262
- Laor, A., & Draine, B. T. 1993, *ApJ*, 402, 441
- Laurent, O., Mirabel, I. F., Charmandaris, V., Gallais, P., Madden, S. C., Sauvage, M., Vigroux, L., & Cesarsky, C. 2000, *A&A*, 359, 887
- La Valley, M., Isobe, T., & Feigelson, E. 1992 in *Astronomical Data Analysis Software and Systems I*, A.S.P. Conf Series, Vol. 25, p. 245 (eds Diana M. Worrall, Chris Biemesderfer, and Jeannette Barnes)
- Lawrence, A., & Elvis, M. 1982, *ApJ*, 256, 410
- Lebofsky, M. J., & Rieke, G. H. 1980, *Nature*, 284, 410
- Le Floc'h, E., Mirabel, I. F., Laurent, O., Charmandaris, V., Gallais, P., Sauvage, M., Vigroux, L., & Cesarsky, C. 2001, *A&A*, 357, 487
- Lira, P., Ward, M., Alexander, D., & Maza, J. 2001, in the *Central Kiloparsec of Starbursts and AGN: The La Palma Connection*, ASP Conference Proceedings Vol. 249, p. 313 (Edited by J. H. Knapen, J. E. Beckman, I. Shlosman, and T. J. Mahoney)
- McAlary, C. W., McLaren, R. A., & Crabtree, D. R. 1979, *ApJ*, 234, 471
- McLeod, K. K., & Rieke, G. H. 1995, *ApJ*, 441, 96
- Maiolino, R., Ruiz, M., Rieke, G. H., & Keller, L. D. 1995, *ApJ*, 446, 561
- Maiolino, R., & Rieke, G. H. 1995, *ApJ*, 454, 95
- Maiolino, R., Marconi, A., Salvati, M., Risaliti, G., Severgnini, P., Oliva, E., La Franca, F., & Vanzì, L. 2001, *A&A*, 365, 28
- Maiolino, R., Marconi, A., & Oliva, E. 2001, *A&A*, 365, 37
- Malkan, M. A., Gorjian, V., & Tam, R. 1998, *ApJS*, 117, 25
- Martini, P., & Pogge, R. W. 1999, *AJ*, 118, 2646
- Martini, P., & Pogge, R. W., Ravindranath, S., & An, J. H. 2001, *ApJ*, 562, 139
- Nenkova, M., Ivezić, Ž., & Elitzur, M. 2002, *ApJ*, 570, L9
- Neugebauer, G., Oke, J. B., Becklin, E. E., & Matthews, K. 1979, *ApJ*, 230, 79
- Osterbrock, D. E. & Martel, A. 1993, *ApJ*, 414, 552
- Pérez García, A. M., & Rodríguez Espinosa, J. M. 2001, *ApJ*, 557, 39
- Pier, E. A., & Krolik, J. H. 1993, *ApJ*, 418, 673
- Pogge, R. W., & Martini, P. 2002, *ApJ*, 569, 624
- Quillen, A. C., Shaked, S., Alonso-Herrero, A., McDonald, C., Lee, A., Rieke, M. J., & Rieke, G. H. 2000, *ApJ*, 532, L17
- Quillen, A. C., McDonald, C., Alonso-Herrero, A., Lee, A., Shaked, S., Rieke, M. J., & Rieke, G. H. 2001, *ApJ*, 547, 129
- Rayner, J. T. et al. 1993, *SPIE*, 1946, 490
- Radomski, J. T., Piña, R. K., Packham, C., Telesco, C. M., De Buizer, J. M., Scott Fisher, R., & Robinson, A. 2002, *ApJ*, in press (astro-ph/0212307)
- Regan, M. W., & Mulchaey, J. S. 1999, *AJ*, 117, 2676
- Rhee, J. H., & Larkin, J. E. 2000, *ApJ*, 538, 98
- Rieke, G. H. 1978, *ApJ*, 226, 550
- Rieke, G. H., & Lebofsky, M. J. 1979, *ApJ*, 227, 710
- Rieke, G. H., & Lebofsky, M. J. 1981, *ApJ*, 250, 87
- Rieke, G. H., & Lebofsky, M. J. 1985, *ApJ*, 288, 618
- Rieke, G. H., & Low, F. J. 1972, *ApJ*, 176, L95
- Rieke, G. H., & Low, F. J. 1975a, *ApJ*, 199, L13
- Rieke, G. H., & Low, F. J. 1975b, *ApJ*, 200, L67
- Rigopoulou, D., Spoon, H. W. W., Genzel, R., Lutz, D., Moorwood, A. F. M., & Tran, Q. D. 1999, *AJ*, 118, 2625
- Risaliti, G., Elvis, M., & Nicastro, F. 2002, *ApJ*, 571, 234
- Roche, P. F., Aitken, D. K., Smith, C. H., & Ward, M. J. 1991, *MNRAS*, 248, 606
- Rudy, R. J., LeVan, P. D., & Rodríguez-Espinoza, J. M. 1982, *AJ*, 87, 598
- Ruiz, M., Rieke, G. H., & Schmidt, G. D. 1994, *ApJ*, 423, 608
- Ruiz, M., Efstathiou, A., Alexander, D. M., & Hough, J. 2001, *MNRAS*, 325, 995
- Rush, B., Malkan, M. A., & Edelson, R. A. 1996, *ApJ*, 473, 130
- Sanders, D. B., Phinney, E. S., Neugebauer, G., Soifer, B. T., & Matthews, K. 1989, *ApJ*, 347, 29
- Schmitt, H. R., Antonucci, R. R. J., Ulvestad, J. S., Kinney, A. L., Clarke, C. J., & Pringle, J. E. 2001, *ApJ*, 555, 663
- Shure, M. A., Toomey, D. W., Rayner, J. T., Onaka, P. M., and Denault, A. J. 1994, *Proc. SPIE*, 2198, 614
- Spinoglio, L., Malkan, M. A. 1989, *ApJ*, 342, 89
- Spinoglio, L., Malkan, M. A., Rush, B., Carrasco, L., & Recillas-Cruz, E. 1995, *ApJ*, 453, 616
- Spoon, H. W. W., Keane, J. V., Tielens, A. G. G. M., Lutz, D., Moorwood, A. F. M., & Laurent, O. 2002, *A&A*, 385, 1022
- Tran, H. D., Osterbrock, D. E., & Martel, A. 1992, *AJ*, 104, 2072
- Tran, H. D. 2001, *ApJ*, 554, L19
- Veilleux, S., Goodrich, R. W., & Hill, G. J. 1997, *ApJ*, 477, 631
- Ward, M., Elvis, M., Fabbiano, G., Carleton, N. P., Willner, S. P., Lawrence, A. 1987, *ApJ*, 315, 74
- Willner, S. P., Elvis, M., Fabbiano, G., Lawrence, A., & Ward, M. J. 1985, *ApJ*, 299, 443
- Young, S., Hough, J. H., Efstathiou, A., Wills, B. J., Bailey, J. A., Ward, M. J., & Axon, D. J. 1996, *MNRAS*, 281, 1206

FIGURE CAPTIONS

Figure 1.— Contours plots of selected galaxies with extended emission in the L -band (right panels). We show the K' -band contour plots for comparison (left panels). The orientation of the images is south up, east to the left.

Figure 2.— *Left panel:* Non-stellar SED of NGC 1068 in units of $\text{erg cm}^{-2} \text{s}^{-1}$. The ISO spectrum of the AGN (nuclear) component of NGC 1068 is from Le Floc'h et al. (2001). The additional mid-infrared data points at 12.6, 17, 22.5, 24.5, and $33.5 \mu\text{m}$ are ground-based small aperture observations from Rieke & Low (1975a); data points at 11.2 and $20.5 \mu\text{m}$ are from Alloin et al. (2000). *Right panel:* Non-stellar SED of NGC 4151 in units of $\text{erg cm}^{-2} \text{s}^{-1}$. The additional mid-infrared data points at 10 and $18 \mu\text{m}$ (unresolved emission) are from Radomski et al. (2002), at $21 \mu\text{m}$ is from Rieke & Low (1972) and at $33.5 \mu\text{m}$ from Rieke & Low (1975b).

Figure 3.— Observed non-stellar SEDs (νf_ν) of optically classified type 1 (1–1.5) CfA Seyferts in units of $\text{erg cm}^{-2} \text{s}^{-1}$.

Figure 4.— Observed non-stellar SEDs (νf_ν) of optically classified intermediate type (1.8–1.9) CfA Seyferts in units of $\text{erg cm}^{-2} \text{s}^{-1}$.

Figure 5.— Observed non-stellar SEDs (νf_ν) of optically classified type 2 CfA Seyferts in units of $\text{erg cm}^{-2} \text{s}^{-1}$.

Figure 6.— Distributions of the fitted spectral indices ($f_\nu \propto \nu^{-\alpha}$) in the optical-infrared wavelengths ($\alpha_{\text{opt-IR}}$ for the spectral range $\simeq 0.4 - 16 \mu\text{m}$, left panels) and infrared wavelengths (α_{IR} for the spectral range $1 - 16 \mu\text{m}$, right panels). The very top panels are the 51 Seyferts in the 'extended' CfA sample with measured spectral indices. The panels below are the same sample broken up in different Seyfert types as derived from optical spectroscopy.

Figure 7.— Effects of foreground extinction ($A_V = 0.4, 1$ and 5 mag) on the observed SED of an AGN, using Rieke & Lebofsky (1985) extinction law. The AGN SEDs are outputs of the Torus+Cone model from Efstathiou & Rowan-Robinson 1995 (see Section 6 and Table 8 for details) for three different viewing angles. $\theta_v = 0^\circ$ is the polar view of the AGN, $\theta_v = 30^\circ$ is an intermediate view (corresponding to the half opening angle of the torus, Θ_c), and $\theta_v = 90^\circ$ is the equatorial view (through the torus).

Figure 8.— Fitted optical-infrared (left panel) and infrared (right panel) spectral indices (see Section 5) as a function of the inclination of the host galaxy, where $b/a = 0$ is an edge-on galaxy, and $b/a = 1$ is a face-on galaxy. The arrows at the top of the plots indicate the values of b/a for the remaining 7 galaxies with no measured spectral indices —dotted lines for the type 2s (green in the on-line version) and solid lines for the type 1s (red in the on-line version). The dashed line indicates a host galaxy axial ratio of $b/a = 0.6$ or an inclination of $i > 53^\circ$ (see discussion in text). The galaxies are separated between Seyfert 1s (1–1.5) shown as open circles (red in the on-line version) and Seyfert 2s (1.8–2) shown as filled star symbols (green in the on-line version), using the classification from optical spectroscopy.

Figure 9.— Predicted infrared spectral indices ($f_\nu \propto \nu^{-\alpha_{\text{IR}}}$) in the $1 - 16 \mu\text{m}$ spectral range as a function of the cosine of the viewing angle to the torus ($\theta_v = 0^\circ$ polar view of the AGN, $\theta_v = 90^\circ$ equatorial view of the AGN) using Efstathiou & Rowan-Robinson (1995) and Efstathiou et al. (1995) torus models. *Left panel:* results for models with a torus half opening angle $\Theta_c = 45^\circ$, and two different equatorial UV optical depths: $\tau_{\text{UV}} = 500 \text{ mag}$ (filled triangles), $\tau_{\text{UV}} = 250 \text{ mag}$ (filled stars), Models Torus 2 and Torus 3 respectively (see Table 8). *Right panel:* results for a torus model with a half opening angle $\Theta_c = 30^\circ$, and an equatorial UV optical depth of $\tau_{\text{UV}} = 1200 \text{ mag}$ with the cone component (Model Torus+Cone in Table 8, open circles) and without the cone component (Model Torus 4 in Table 8, filled circles). In both diagrams the shaded areas represent the observed ranges of fitted α_{IR} for Seyfert 1–1.5s (darkest shaded area), Seyferts 1.8–1.9s (intermediate shaded area), and Seyfert 2s (lightest shaded area) in the CfA sample.

TABLE 1
SUMMARY OF HIGH RESOLUTION OPTICAL, NEAR-INFRARED AND MID-INFRARED OBSERVATIONS FOR THE CFA
SEYFERT GALAXIES.

Galaxy (1)	Type (2)	WFPC1/2 (3)	Ref (4)	NICMOS (5)	Ref (6)	KL (7)	Mid-IR (8)	Ref (9)
Mkn 334	Sy1.8	*	1	F110W, F160W	2, 4	2	6.75, 9.63, 10, 16 μ m	5, 9, 6
Mkn 335	Sy1.0	F785LP	1	2	6.75, 9.63, 16 μ m	5, 6
UGC 524/0048+29	Sy1.0	10 μ m	9
I Zw 1	Sy1.0	F555W	1	10	5.9, 7.7, 10, 16 μ m	7, 10, 6
Mkn 993	Sy1.5 – 2.0	F606W	1	2	10, 16 μ m	11, 6
Mkn 573	Sy2.0 (non-HBLR)	F708W	2	F110W, F160W	2, 4	3	10, 16 μ m	11, 6
UM 146/UGC 1395	Sy1.9	F606W	1	F110W, F160W	2, 4	2	6.75, 10, 16 μ m	2, 9, 6
Mkn 590/NGC 863	Sy1.0	F785LP	1	2	6.75, 9.63, 16 μ m	5, 6
NGC 1068	Sy2.0/Sy1.8 (HBLR)	F110W, F160W	3	3	5 – 16, 16 μ m	13, 6
NGC 1144	Sy2.0 (non-HBLR)	F606W	2	F110W, F160W	2, 4	2	6.75, 10, 16 μ m	2, 11, 6
Mkn 1243/NGC 3080	Sy1.0	10, 16 μ m	9, 6
NGC 3227	Sy1.5	F547M	1	F160W, F222M	3	2	6.75, 9.63, 16 μ m	5, 6
NGC 3362	Sy2.0 (non-HBLR)	F606W	2	F110W, F160W	2, 4	2	10, 16 μ m	9, 6
UGC 6100	Sy2.0 (non-HBLR)	F606W	2	F110W, F160W	2, 4	2	6.75, 9.63, 10, 16 μ m	5, 9, 6
NGC 3516	Sy1.5	F547M	1	F160W	4	14	6.75, 9.63, 16 μ m	5, 6
NGC 3786/Mkn 744	Sy1.8	*	1	F110W, F160W	2, 4	2	10, 16 μ m	9, 6
NGC 3982	Sy2.0/Sy1.9 (non-HBLR)	F606W	2	F110W, F160W	2, 4	2	6.75, 9.63, 10, 16 μ m	5, 9, 6
NGC 4051	Sy1.0	F547M	1	2	6.75, 9.63, 10, 16 μ m	5, 10, 6
NGC 4151	Sy1.5	F547M	1	F110W, F160W	3	3	5.9, 7.7, 10, 16 μ m	7, 10, 6
NGC 4235	Sy1.0	F547M	1	F222M F160W	4	2	10, 16 μ m	9, 6
NGC 4253/Mkn 766	Sy1.5	F785LP	1	F160W	4	2	6.75, 9.63, 10, 16 μ m	5, 9, 6
Mkn 205	Sy1.0	F814W	1	10	6.75, 10, 16 μ m	2, 16, 6
NGC 4388	Sy2.0/Sy1.9 (HBLR)	F110W, F160W	2, 4	8	6.75, 9.63, 10, 16 μ m	5, 17, 6
NGC 4395	Sy1.0/Sy1.8	F450W	1	F160W	4	2	10, 12 μ m	9, 15
Mkn 231	Sy1.0	F814W	1	F110W, F160W	2, 4	10	5.9, 7.7, 10, 16 μ m	7, 10, 6
NGC 5033	Sy1.9/Sy1.5	F547M	2	F110W, F160W	2, 4	2	6.75, 9.63, 10, 16 μ m	5, 9, 6
UGC 8621/1335+39	Sy1.8	6.75, 9.63, 16 μ m	5, 6
NGC 5252	Sy1.9 (HBLR)	F547M	2	F110W, F160W	2, 4	3	6.75, 9.63, 10, 16 μ m	3, 9
NGC 5256/Mkn 266SW	Sy2.0 (non-HBLR)	F110W, F160W	2, 4	2	6.75, 9.63, 10, 16 μ m	5, 9, 6
NGC 5283/Mkn 270	Sy2.0 (non-HBLR)	F708W	2	F110W, F160W	2, 4	2	6.75, 10, 16 μ m	2, 10, 6
NGC 5273	Sy1.9/Sy1.5	F439W	2	F110W, F160W	2, 4	2	6.75, 9.63, 10, 16 μ m	5, 9, 6
Mkn 461	Sy2.0	F110W, F160W	2, 4	2	6.75, 10 μ m	2, 9
NGC 5347	Sy2.0 (non-HBLR)	F110W, F160W	2, 4	2	10 μ m	9
Mkn 279	Sy1.0	*	1	10	6.75, 9.63, 16 μ m	5, 6
NGC 5548	Sy1.5	F785LP	1	F160W, F222M	3	2	6.75, 9.63, 16 μ m	5, 6
Mkn 471	Sy1.8	F606W	1	F110W, F160W	2, 4	10	10 μ m	10
NGC 5674	Sy1.9	F606W	1	F110W, F160W	2, 4	2	6.75, 9.63, 10 μ m	5, 9
Mkn 817	Sy1.5	F785LP	1	12	6.75, 9.63, 16 μ m	5, 6
NGC 5695/Mkn 686	Sy2.0 (non-HBLR)	F606W	2	F110W, F160W	2, 4	...	10, 12 μ m	9, 2
Mkn 841	Sy1.5	F785LP	1	2	6.75, 9.63, 10, 16 μ m	5, 9, 6

TABLE 1—*Continued*

Galaxy (1)	Type (2)	WFPC1/2 (3)	Ref (4)	NICMOS (5)	Ref (6)	<i>KL</i> (7)	Mid-IR (8)	Ref (9)
NGC 5929	Sy2.0 (non-HBLR)	F606W	2	F110W, F160W	2, 4	2	6.75, 9.63, 10, 16 μ m	5, 9, 6
NGC 5940	Sy1.0	F606W	1	F160W	4	2	6.75, 9.63, 10 μ m	2, 9
Mkn 1513	Sy1.0	2	6.75, 10, 14.3 μ m	2, 10
NGC 6104	Sy1.5 – 1.8	F606W	1	F160W	4	...	10, 16 μ m	9, 6
UGC 12138	Sy1.8	*	1	F110W, F160W	2, 4	2	6.75, 9.63, 10, 16 μ m	2, 9, 6
NGC 7469	Sy1.0	F785LP	1	F110W, F160W F222M	3	2	6.75, 10, 16 μ m	8, 10, 6
NGC 7603/Mkn 530	Sy1.5/Sy1.8	F785LP	1	2	6.75, 9.63, 10 μ m	5, 10
NGC 7674/Mkn 533	Sy2.0 (HBLR)	F110W, F160W	2, 4	3	6.75, 9.63, 10, 16 μ m	5, 9, 6
NGC 7682	Sy2.0 (HBLR)	F606W	2	F110W, F160W	2, 4	2	6.75, 10, 16 μ m	2, 9, 6

NOTE.—Column (2): Seyfert types taken from Osterbrock & Martel (1993) and Ho et al. (1997). NGC 6104 has been classified as a Seyfert 1.5 – 1.8 galaxy by Jiménez-Benito et al. (2000). Goodrich (1995) reports that NGC 7603/Mkn 530 and Mkn 993 (see also Tran, Osterbrock, & Martel 1992) have undergone transitions between types Seyfert 1 and Seyfert 1.8 – 1.9. We also indicate in this column for the Seyfert 2s whether hidden broad line regions have been detected from spectropolarimetry (HBLR) or not (non-HBLR). Column (3): *HST* optical filter, unless the * symbol is used in which case the optical unresolved flux was estimated from ground-based observation (see Ho & Peng (2001) for more details). Column (4): references for the unresolved optical fluxes. Column (5): *HST*/NICMOS filters. Column (6): references for the NICMOS fluxes. Column (7): references for the *KL*-band fluxes. Column (8): Mid-infrared data available. 5.9, 6.75, 7.7, 9.63, 12.5, 14.3 and 16 μ m indicate *ISO* data, and 10 μ m indicates ground-based *N*-band measurements. Column (9): references for the mid-infrared fluxes. References in Columns (4), (6), (7) and (9): 1. Ho & Peng (2001). 2. This work. 3. Alonso-Herrero et al. (2001). 4. Quillen et al. (2001) 5. Clavel et al. (2000). 6. Pérez García & Rodríguez Espinosa (2001). 7. Rigopoulou et al. (1999). 8. Alonso-Herrero et al. (1998). 9. Maiolino et al. (1995). 10. Rieke (1978). 11. Edelson et al. (1987). 12. Rudy, LeVan, & Rodríguez-Espinosa (1982). 13. Le Floc'h, private communication (2002). 14. McAlary, McLaren, & Crabtree (1979). 15. Bendo et al. (2002). 16. Neugebauer et al. (1979). 17. Scoville et al. (1983).

TABLE 2

SUMMARY OF HIGH RESOLUTION OPTICAL, NEAR-INFRARED AND MID-INFRARED OBSERVATIONS FOR ADDITIONAL SEYFERT GALAXIES IN THE CFA SAMPLE.

Galaxy (1)	Type (2)	WFPC1/2 (3)	Ref (4)	NICMOS (5)	Ref (6)	<i>KL</i> band (7)	Mid-infrared (8)	Ref (9)
NGC 3031	Sy1.5	F547M	1	F160W	2	9	10 μ m	10
NGC 3079	Sy2.0	F160W	2	9	10, 16 μ m	6, 7
NGC 3185	Sy2.0:	10, 12 μ m	11, 4
NGC 4258	Sy1.9	F547M	1	F110W, F160W, F222M	3	3	10.5, 12.5, 17.9 μ m	3
NGC 4501	Sy2.0	9	10 μ m	6
NGC 4579	Sy1.9/L1.9	F547M	1	4	6.75, 9.63 μ m	5
NGC 5194	Sy2.0	F110W, F160W, F222M	2, 4	8	9.55, 12.5 μ m	4
NGC 7479	Sy1.9	F569W	1	F160W	2	4	6.75, 10, 14.3 μ m	4, 9
NGC 7743	Sy2.0	F160W	2	4

NOTE.—See Table 1 for an explanation. Column (2): the Seyfert types are from Ho et al. (1997). Column (8): the mid-IR fluxes of NGC 4258 are ground-based. References in Columns (4), (6), (7) and (9): 1. Ho & Peng (2001). 2. Quillen et al. (2001) 3. Chary et al. (2000). 4. This work. 5. Clavel et al. (2000). 6. Devereux (1987). 7. Pérez García & Rodríguez Espinosa (2001). 8. Ellis, Gondhalekar, & Efstathiou (1982). 9. Willner et al. (1985). 10. Rieke & Lebofsky (1978). 11. Maiolino et al. (1995).

TABLE 3
DISTRIBUTION OF TYPE 1S AND TYPE 2S IN DIFFERENT
SAMPLES.

Sample (1)	No. galaxies (2)	Type 1 (3)	Type 2 (4)
<i>All b/a</i>			
Extended CfA	58	43%	57%
RSA	60	28%	72%
Palomar*	44	27%	73%
12 μm	55	45%	55%
<i>$b/a \geq 0.6$</i>			
Extended CfA	47	43%	57%
RSA	41	37%	63%
Palomar*	32	28%	72%
12 μm	39	56%	44%

NOTE.—Distribution of type 1 ($1 - 1.5$) and type 2 ($1.8 - 2$) Seyferts based on their optical classification.

* Only galaxies with certain Seyfert classification are included.

TABLE 4
IRTF $K'L$ -BAND APERTURE PHOTOMETRY AND L-BAND UNRESOLVED CONTRIBUTION WITHIN
A $3''$ -DIAMETER APERTURE.

Galaxy (1)	FWHM (2)	Aperture (3)	K' (4)	$K' - L$ (5)	$\frac{f_{\text{unresolved}}}{f_{3''}}$ (6)	L-band Morphology (7)
Mkn 334	0.78	1.5	11.64	1.53	89%	Compact
		3	11.21	1.44		
		6	10.97	1.32		
		9	10.83	...		
Mkn 335	0.72	1.5	10.88	1.76	94%	Compact
		3	10.60	1.76		
		6	10.50	1.72		
		9	10.46	...		
UM 146/UGC 1395	0.84	1.5	13.19	1.21	65%	Compact
		3	12.63	1.10		
		6	12.25	0.82		
		9	12.00	...		
Mkn 590	0.86	1.5	11.96	2.25	76%	Compact
		3	11.38	1.95		
		6	11.00	1.68		
			10.80	...		
Mkn 993	...	6	11.40	0.36	...	Blind offsets
NGC 1144	1.11	1.5	13.19	1.14	40%	Extended
		3	12.22	0.84		
		6	11.51	0.60		
		9	11.05	0.52		
UGC 6100	...	6	12.23	0.23	...	Blind offsets
NGC 3227	0.81	1.5	10.87	1.37	71%	Compact
		3	10.24	1.15		
		6	9.82	0.91		
		9	9.62	0.76		
NGC 3362	...	6	12.80	0.40	...	Blind offsets
NGC 3786/Mkn 744	1.08	6	10.74	1.07	56%	Tracking problems
NGC 3982	...	6	12.67	1.17	...	Blind Offsets
NGC 4051	0.78	1.5	10.54	1.59	73%	Compact
		3	10.08	1.44		
		6	9.80	1.30		
		9	9.67	1.21		
NGC 4235	1.05	1.5	12.26	1.03	58%	Extended
		3	11.44	0.76		
		6	10.77	0.46		
		9	10.37	0.24		
NGC 4253/Mkn 766	0.69	1.5	11.37	1.87	90%	Compact
		3	10.96	1.75		
		6	10.70	1.60		
		9	10.55	1.50		
NGC 4395	...	6	14.00	1.29	...	Blind Offsets
NGC 4579	1.02	1.5	11.28	0.49	45%	Extended
		3	10.32	0.33		
		6	9.57	0.22		
		9	9.17	0.15		
NGC 5033	0.98	1.5	11.59	0.66	35%	Extended
		3	10.59	0.42		
		6	9.77	0.26		
		9	9.31	0.19		

TABLE 4—*Continued*

Galaxy (1)	FWHM (2)	Aperture (3)	K' (4)	$K' - L$ (5)	$\frac{f_{\text{unresolved}}}{f_{3''}}$ (6)	L -band Morphology (7)
NGC 5256/Mkn 266SW	—	1.5	13.21	0.93	16%	Extended
		3	12.30	0.98		
		6	11.71	0.94		
		9	11.44	...		
NGC 5256/Mkn 266NE*	—	1.5	13.51	0.58	...	Extended
		3	12.67	0.65		
		6	12.08	0.67		
		9	11.77	...		
NGC 5273	1.6?	1.5	12.98	0.64	38%	Extended
		3	11.92	0.48		
		6	11.17	0.27		
		9	10.83	...		
NGC 5283/Mkn 270	—	6	11.26	0.22	...	Blind Offsets
Mkn 461	—	6	$L = 11.97$	Blind Offsets
NGC 5347	0.75	1.5	12.80	2.09	65%	Compact
		3	12.09	1.80		
		6	11.62	1.51		
		9	11.34	1.30		
NGC 5548	0.84	1.5	11.26	1.93	65%	Compact
		3	10.77	1.82		
		6	10.46	1.66		
		9	10.29	1.53		
NGC 5674	0.83	1.5	12.69	1.41	57%	Compact
		3	12.09	1.30		
		6	11.66	1.12		
		9	11.43	1.03		
Mkn 841	0.90	1.5	12.88	2.10	57%	Compact
		3	12.34	2.04		
		6	12.10	1.97		
		9	11.98	1.92		
NGC 5929	1.50	1.5	13.07	0.43	16%	Extended
		3	12.13	0.27		
		6	11.45	0.04		
NGC 5930*	1.95	1.5	12.37	0.63		Extended
		3	11.41	0.63		
		6	10.86	0.43		
		9	10.57	0.28		
NGC 5940	...	1.5	13.95	Not detected
		3	13.11			
		6	12.52			
		9	12.18			
Mkn 1513	0.77	1.5	11.23	1.68	75%	Compact
		3	10.89	1.67		
		6	10.78	1.66		
UGC 12138	0.86	1.5	12.39	1.36	54%	Compact
		3	11.81	1.21		
		6	11.46	1.07		
		9	11.29	0.98		

TABLE 4—*Continued*

Galaxy (1)	FWHM (2)	Aperture (3)	K' (4)	$K' - L$ (5)	$\frac{f_{\text{unresolved}}}{f_{3''}}$ (6)	L -band Morphology (7)
NGC 7469	0.75	1.5	11.17	1.96	71%	Compact nucleus + Extended
		3	10.41	1.64		
		6	9.90	1.42		
		9	9.73	1.34		
NGC 7479	0.75	1.5	12.78	1.59	61%	Compact nucleus + Extended
		3	11.95	1.22		
		6	11.19	0.83		
		9	10.74	0.64		
NGC 7603/Mkn 530	0.69	1.5	10.85	1.59	100%	Compact
		3	10.45	1.48		
		6	10.21	1.37		
		9	10.07	1.27		
NGC 7682	...	6	11.92	0.05	...	Blind Offsets
NGC 7743	1.00	1.5	11.93	0.16	< 45%	Extended
		3	11.22	0.19		
		6	10.67	0.20		
		9	10.38	0.25		

NOTE.—Column (1): Galaxy. Column (2): Size (FWHM) of the nucleus as measured from the L -band image. Column (3): Diameter in arcsec of the circular apertures used for the photometry. Column (4): K' -band magnitude. Column (5): measured $K' - L$ color. Column (6): Fraction of unresolved emission within a $3''$ -diameter aperture in the L -band. Column (7): Morphology of the L -band emission.

* NGC 5930 and Mkn 266NE are not part of the CfA sample of Seyfert galaxies.

TABLE 5
GALAXIES WITH CIRCUMNUCLEAR RADIO AND MID-INFRARED EMISSION.

Galaxy (1)	6 cm $\frac{f_{0.3''}}{f_{15''}}$ (2)	10 μm $\frac{f_{\text{ground}}}{f_{\text{ISO}}}$ (3)	Extended L (4)	Extended ISO (5)
Mkn 334	0.12	1.18	no	no
NGC 1144	0.07	...	yes	yes (at $6.75 \mu\text{m}$)
NGC 3982	0.03	0.34	...	yes
NGC 4051	0.07	0.77	no	no
NGC 4388	0.08	1.90	no	yes + bright point source
NGC 5033	0.15	0.19	yes	yes
NGC 5256/Mkn 266SW	0.10	0.33	yes	yes + bright point source
Mkn 841	0.14	1.28	no	no
NGC 5929	0.40	0.41	yes	yes
NGC 5940	...	0.45	...	yes

NOTE.—Column (1): Galaxy. Column (2): Ratio of the nuclear ($0.3''$) to extended ($15''$) emission at 6 cm. Column (3): Ratio of ground-based to ISO fluxes at $10 \mu\text{m}$. Column (4) and Column (5) indicate whether there is evidence for significant extended emission from the IRTF L -band images and ISO $9.63 \mu\text{m}$ images, respectively.

TABLE 6

NUCLEAR (UNRESOLVED) OPTICAL AND INFRARED FLUXES FOR SEYFERT 1.8 – 2 GALAXIES IN THE EXTENDED CFA SAMPLE, AND FITTED SPECTRAL INDICES.

Galaxy (1)	f_{opt} (2)	$f_{1.1}$ (3)	$f_{1.6}$ (4)	$f_{2.1}$ (5)	$f_{3.5}$ (6)	$f_{6.75}$ (7)	f_{10} (9)	f_{16} (9)	$\alpha_{\text{opt-IR}}$ (10)	α_{IR} (11)
Mkn 334	< 3.8	2.33	6.83	13.8	31.7	131.	148.	< 390.	1.80 ± 0.11	1.80 ± 0.11
Mkn 573	< 0.097	0.15	0.54	3.2	18.8	...	167.*	< 550.	2.98 ± 0.20	2.91 ± 0.23
UM 146/UGC 1395	0.090	0.35	0.82	3.0	4.4	15.	15.*	< 250.	1.98 ± 0.18	1.76 ± 0.18
NGC 1068	...	9.8	98.	445.	3080.	13600.	19600.	< 46900.	3.02 ± 0.31	3.02 ± 0.31
NGC 1144	< 0.020	< 0.11	0.08	...	3.4	< 120.	< 158.*	< 460.	3.3	3.3
NGC 3079	< 0.1	...	< 61	...	92.*	< 2070	3.7	3.7
NGC 3185	20.*
NGC 3362	< 0.031	0.04	0.05	...	< 2.2	...	12.*	< 210.	2.75 ± 0.20	2.75 ± 0.20
UGC 6100	< 0.053	< 0.17	< 0.15	...	< 4.6	42.	46.	< 130.	3.4	3.4
NGC 3786/Mkn 744	2.2	1.75	3.25	< 11.9	17.7	...	59.*	< 190.	1.22 ± 0.19	1.65 ± 0.09
NGC 3982	0.009	< 0.27	0.34	...	< 7.2	< 62.	19.*	< 430.	2.77 ± 0.19	2.4
NGC 4258	< 0.019	< 0.5	0.9	4.0	20.	...	100.*	...	2.85 ± 0.30	2.39 ± 0.21
NGC 4388	...	0.06	0.71	...	39.9	265.	267.	< 1550.	3.51 ± 0.42	3.51 ± 0.42
NGC 4501	< 35	17.*
NGC 4579	0.202	< 14	12.5	104.	113.	...	2.30 ± 0.13	2.35 ± 0.46
NGC 5033	0.89	0.61	3.22	< 8.0	8.6	< 179.	24.*	< 1340.	1.41 ± 0.20	1.67 ± 0.22
NGC 5194	...	< 0.14	0.19	0.38	< 34.	...	110.	...	3.78 ± 0.11	3.78 ± 0.11
UGC 8621/1335+39	49.	49.	< 130.
NGC 5252	0.070	0.20	0.70	1.0	11.1	15.	27.	< 45.	2.03 ± 0.20	1.94 ± 0.26
NGC 5256/Mkn 266SW	...	< 0.08	< 0.15	...	2.4	< 125.	30.*	< 330.	3.0	3.0
NGC 5283/Mkn 270	< 0.013	< 0.43	< 0.30	...	< 11.0	< 11.	17.*	< 60.	2.7	2.7
NGC 5273	0.27	0.68	1.67	...	3.0	23.	25.	< 90.	1.63 ± 0.11	1.66 ± 0.15
Mkn 461	...	< 0.45	< 0.46	...	< 4.7	< 12.	12.*	...	1.8	1.8
NGC 5347	...	0.22	0.97	4.0	14.3	...	208.*	...	3.06 ± 0.18	3.06 ± 0.18
Mkn 471	0.15	0.18	0.32	...	3.0	...	14.*	...	1.82 ± 0.18	2.08 ± 0.14
NGC 5674	0.11	0.90	2.62	4.2	7.5	38.	43.	...	2.08 ± 0.16	1.78 ± 0.11
NGC 5695/Mkn 686	< 0.039	< 0.17	< 0.25	< 10.*
NGC 5929	< 0.023	< 0.17	< 0.25	...	1.3	< 41.	24.*	< 550.	2.9	2.9
UGC 12138	< 2.4	1.86	2.59	5.3	9.0	40.	54.	< 250.	1.64 ± 0.08	1.64 ± 0.08
NGC 7479	< 0.006	...	0.24	< 3.	9.0	150.	263.*	...	3.85 ± 0.24	3.58 ± 0.30
NGC 7674/Mkn 533	...	1.25	5.0	12.3	53.	259.	344.	< 860.	2.36 ± 0.18	2.36 ± 0.18
NGC 7682	< 0.04	< 0.10	< 0.13	...	< 4.8	10.	12.*	< 290.	3.0	3.1
NGC 7743	< 0.5	< 8.	< 5.

NOTE.— This table contains all the optically classified Seyfert 1.8 – 2 galaxies in the 'extended' CFA sample. The measured unresolved flux densities in Columns (2) through (9) are listed in mJy. Columns (10) and (11) are the fitted spectral indices ($f_\nu \propto \nu^{-\alpha}$) in the optical-infrared ($\alpha_{\text{opt-IR}}$, spectral range $\simeq 0.4 - 16 \mu\text{m}$) and infrared (α_{IR} , spectral range $1 - 16 \mu\text{m}$), respectively. If no optical measurement is available, we give the same value for $\alpha_{\text{opt-IR}}$ and α_{IR} . When the errors are not quoted for the fitted spectral indices it means that the formal errors are infinity (those cases with only two or fewer detections).

Column (9) * indicates small aperture ground-based N -band measurement (see discussion in Section 4.3). The ground-based N -band fluxes (derived to give monochromatic fluxes of Rayleigh-Jeans spectra) need to be corrected to $\nu f_\nu = \text{constant}$ by multiplying them by a factor of 1.22 (see also Edelson et al. 1987, and Section 5).

Additional nuclear fluxes at $4.8 \mu\text{m}$ (ground-based) — Mkn 573: 41.3 mJy; NGC 1068: 8245 mJy; NGC 5252: 15.7 mJy; NGC 7674/Mkn 533: 108.6 mJy (Alonso-Herrero et al. 2001). Additional nuclear fluxes at $12 \mu\text{m}$ (ISO) — NGC 3185: 20 mJy; NGC 5194: 400 mJy; NGC 5695/Mkn 686: < 55 mJy. Additional nuclear fluxes at $12 \mu\text{m}$ (ground-based): NGC 4258: 165 mJy. Additional nuclear fluxes at $14.3 \mu\text{m}$ (ISO) — NGC 7479: 520 mJy. Additional nuclear fluxes at $17.9 \mu\text{m}$ (ground-based) — NGC 4258: 300 mJy.

TABLE 7

NUCLEAR (UNRESOLVED) OPTICAL AND INFRARED FLUXES FOR SEYFERT 1 – 1.5 GALAXIES IN THE EXTENDED CFA SAMPLE.

Galaxy (1)	f_{opt} (2)	$f_{1.1}$ (3)	$f_{1.6}$ (4)	$f_{2.1}$ (5)	$f_{3.5}$ (6)	$f_{6.75}$ (7)	f_{10} (9)	f_{16} (9)	$\alpha_{\text{opt-IR}}$ (10)	α_{IR} (11)
Mkn 335	4.0	32.8	78.2	155.	203.	< 240.	1.31 ± 0.18	0.93 ± 0.15
UGC 524/0048+29	41.*
Mkn 993	0.039	< 3.1	< 11.	...	18.*	< 130.	2.2	1.6
I Zw 1	2.20	110.	...	310.*	< 640.	1.64 ± 0.14	1.07 ± 0.10
Mkn 590	0.80	9.3	38.0	144.	198.	< 460.	2.08 ± 0.14	1.81 ± 0.17
Mkn 1243	16.*	< 210.
NGC 3031	1.39	...	13.4	< 202.	< 161.	...	86.*	...	1.42 ± 0.15	1.1
NGC 3227	2.70	...	10.6	22.6	46.7	294.	382.	< 1220.	1.80 ± 0.10	1.97 ± 0.11
NGC 3516	2.20	...	18.1	...	117.	264.	369.	< 770.	1.71 ± 0.11	1.51 ± 0.16
NGC 4051	1.60	38.2	73.5	265.	411.	< 1440.	1.91 ± 0.08	1.62 ± 0.07
NGC 4151	51.4	69.0	103.6	177.5	325.	...	1400.*	< 4120.	1.26 ± 0.08	1.44 ± 0.03
NGC 4235	0.44	...	3.69	< 6.6	9.0	...	34.*	< 170.	1.51 ± 0.09	1.30 ± 0.04
NGC 4253/Mkn 766	3.90	...	20.0	20.3	58.0	177.	274.	< 730.	1.65 ± 0.07	1.56 ± 0.08
Mkn 205	2.10	13.	30.	58.*	< 190.	1.34 ± 0.06	1.53 ± 0.10
NGC 4395	0.17	...	0.85	< 1.1	< 2.4	...	12.*	...	1.29 ± 0.10	1.5
Mkn 231	16.3	...	80.1	...	326.	...	1420.*	< 3960.	1.73 ± 0.07	1.59 ± 0.06
Mkn 279	4.2	32.	102.	146.	< 290.	1.14 ± 0.06	1.38 ± 0.11
NGC 5548	4.3	...	15.0	31.6	46.2	177.	268.	< 440.	1.52 ± 0.09	1.43 ± 0.10
Mkn 817	2.2	55.	142.	259.	< 490.	1.78 ± 0.11	1.43 ± 0.05
Mkn 841	1.8	4.1	12.0	74.	133.	< 340.	1.75 ± 0.17	2.18 ± 0.12
NGC 5940	0.46	...	0.93	< 1.9	...	< 46.	26*	...	1.54 ± 0.18	1.8
Mkn 1513	19.7	44.6	85.	140.*	...	1.08 ± 0.12	1.08 ± 0.12
NGC 6104	0.12	...	0.13	12.*	< 120.	1.76 ± 0.35	2.5
NGC 7469	6.4	16.2	39.0	67.8	90.	433.	600.	< 1290.	1.67 ± 0.09	1.57 ± 0.09
NGC 7603/Mkn 530	0.53	21.	74.0	138.	176.*	...	2.29 ± 0.32	1.35 ± 0.19

NOTE.—This table contains all the optically classified Seyfert 1 – 1.5 galaxies in the 'extended' CFA sample. The measured unresolved flux densities in Columns (2) through (9) are listed in mJy. Columns (10) and (11) are the fitted spectral indices ($f_\nu \propto \nu^{-\alpha}$) in the optical-infrared ($\alpha_{\text{opt-IR}}$, spectral range $\simeq 0.4 - 16 \mu\text{m}$) and infrared (α_{IR} , spectral range $1 - 16 \mu\text{m}$), respectively. If no optical measurement is available, we give the same value for $\alpha_{\text{opt-IR}}$ and α_{IR} . When the errors are not quoted for the fitted spectral indices it means that the formal errors are infinity (those cases with only two or fewer detections).

Column (9) * indicates small aperture ground-based N -band measurement (see discussion in Section 4.3). The ground-based N -band fluxes (derived to give monochromatic fluxes of Rayleigh-Jeans spectra) need to be corrected to $\nu f_\nu = \text{constant}$ by multiplying them by a factor of 1.22 (see also Edelson et al. 1987, and Section 5).

Additional fluxes at $5.5 \mu\text{m}$ (ISO) — I Zw 1: 173 mJy, NGC 4151: 882 mJy, Mkn 231: 606 mJy. Additional fluxes at $7.7 \mu\text{m}$ (ISO) — I Zw 1: 221 mJy, NGC 4151: 1090 mJy, Mkn 231: 919 mJy. Additional fluxes at $12 \mu\text{m}$ (ISO) — NGC 4395: 7.6 mJy. Additional fluxes at $14.3 \mu\text{m}$ (ISO) — Mkn 1513: 160 mJy.

TABLE 8

PARAMETERS OF EFSTATHIOU & ROWAN-ROBINSON (1995) AND EFSTATHIOU ET AL. (1995) TORUS MODELS.

Model (1)	Θ_c (2)	τ_{UV} (3)	r_1/r_2 (4)	h/r_2 (5)	T (6)
Torus 1	45°	1000	0.05	0.5	1000
Torus 2	45°	500	0.05	0.5	1000
Torus 3	45°	250	0.05	0.5	1000
Torus 4	30°	1200	0.01	0.1	900
Torus+Cone	30°	1200	0.01	0.1	900

NOTE.—Column (2): Θ_c is the half opening angle of the torus. Column (3): τ_{UV} is the equatorial UV optical depth in magnitudes. Column (4): r_1/r_2 is ratio of the inner and outer torus radii. Column (5): h/r_2 is the ratio of the height scale and the outer radius. Column (6): T (in K) is the dust sublimation temperature.

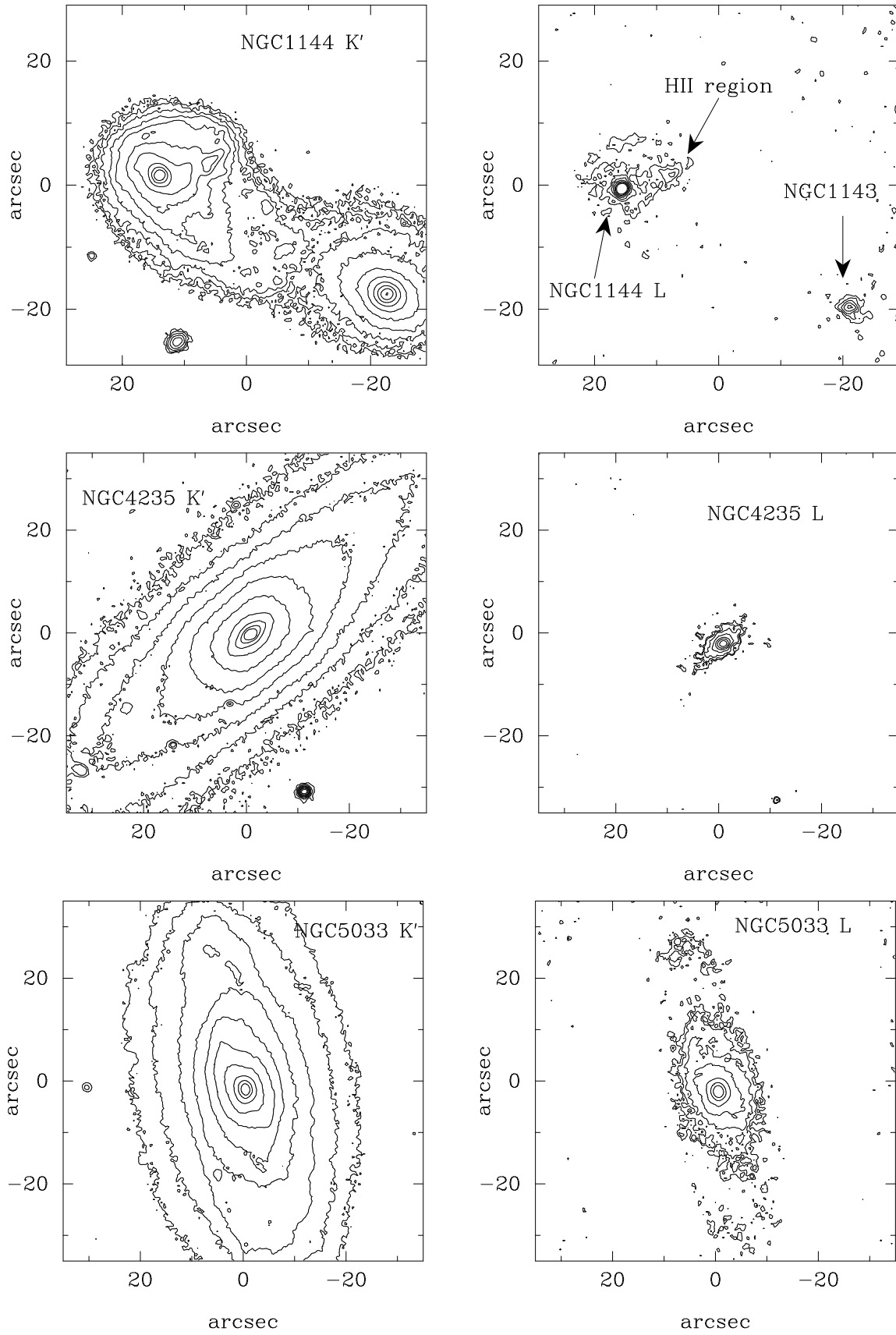


FIG. 1.— Contours plots of selected galaxies with extended emission in the L -band (right panels). We show the K' -band contour plots for comparison (left panels). The orientation of the images is south up, east to the left.

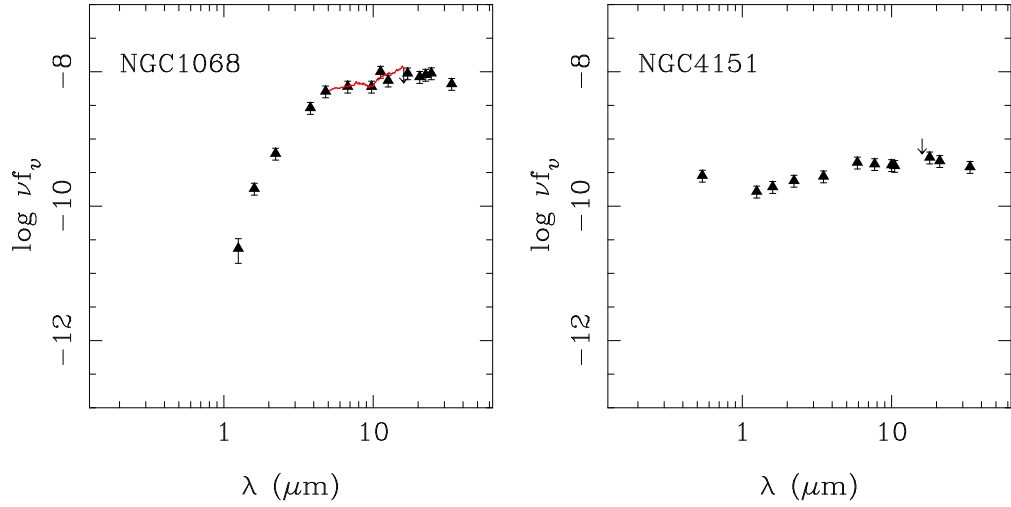


FIG. 2.— *Left panel:* Non-stellar SED of NGC 1068 in units of $\text{erg cm}^{-2} \text{s}^{-1}$. The *ISO* spectrum of the AGN (nuclear) component of NGC 1068 is from Le Floc'h et al. (2001). The additional mid-infrared data points at 12.6, 17, 22.5, 24.5, and $33.5 \mu\text{m}$ are ground-based small aperture observations from Rieke & Low (1975a); data points at 11.2 and $20.5 \mu\text{m}$ are from Alloin et al. (2000). *Right panel:* Non-stellar SED of NGC 4151 in units of $\text{erg cm}^{-2} \text{s}^{-1}$. The additional mid-infrared data points at 10 and $18 \mu\text{m}$ (unresolved emission) are from Radomski et al. (2002), at $21 \mu\text{m}$ is from Rieke & Low (1972) and at $33.5 \mu\text{m}$ from Rieke & Low (1975b).

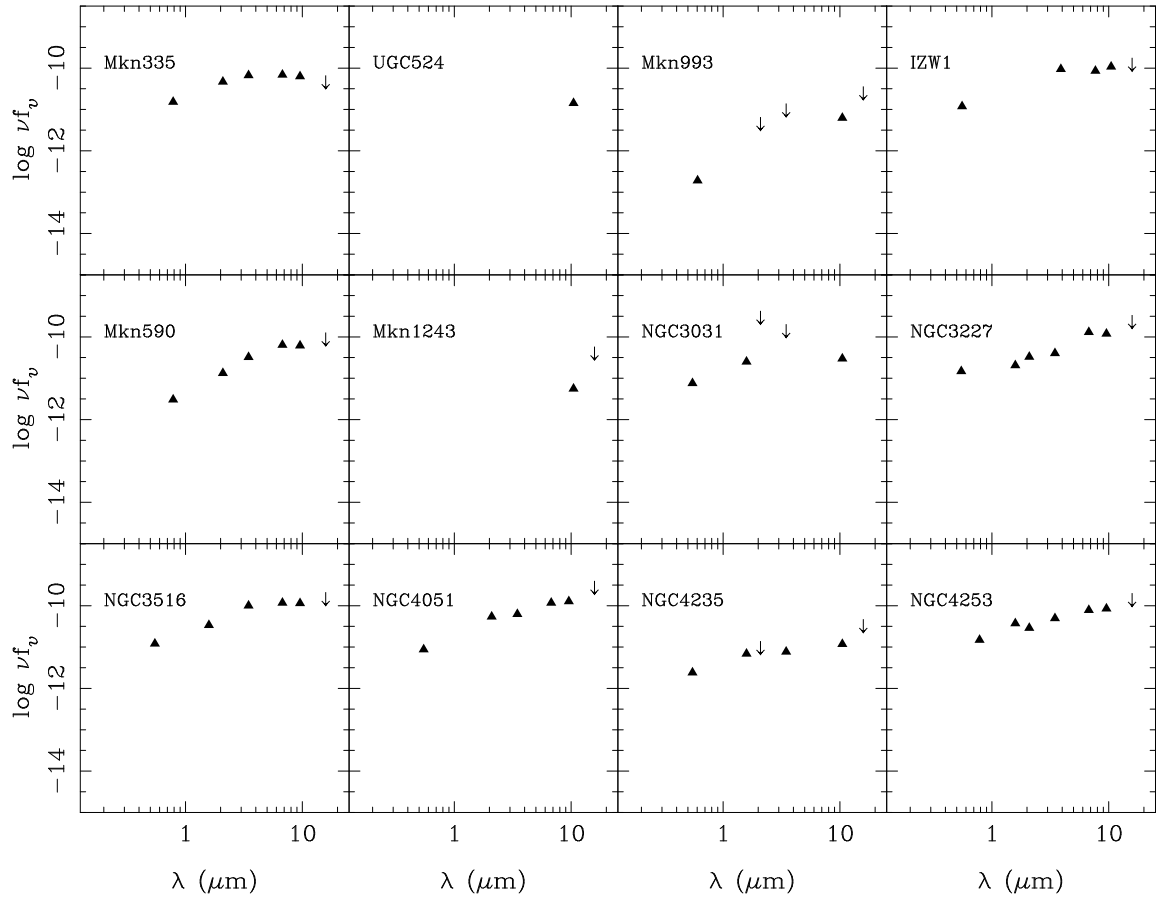


FIG. 3A.— Observed non-stellar SEDs (νf_ν) of optically classified type 1 (1 – 1.5) CfA Seyferts in units of $\text{erg cm}^{-2} \text{s}^{-1}$.

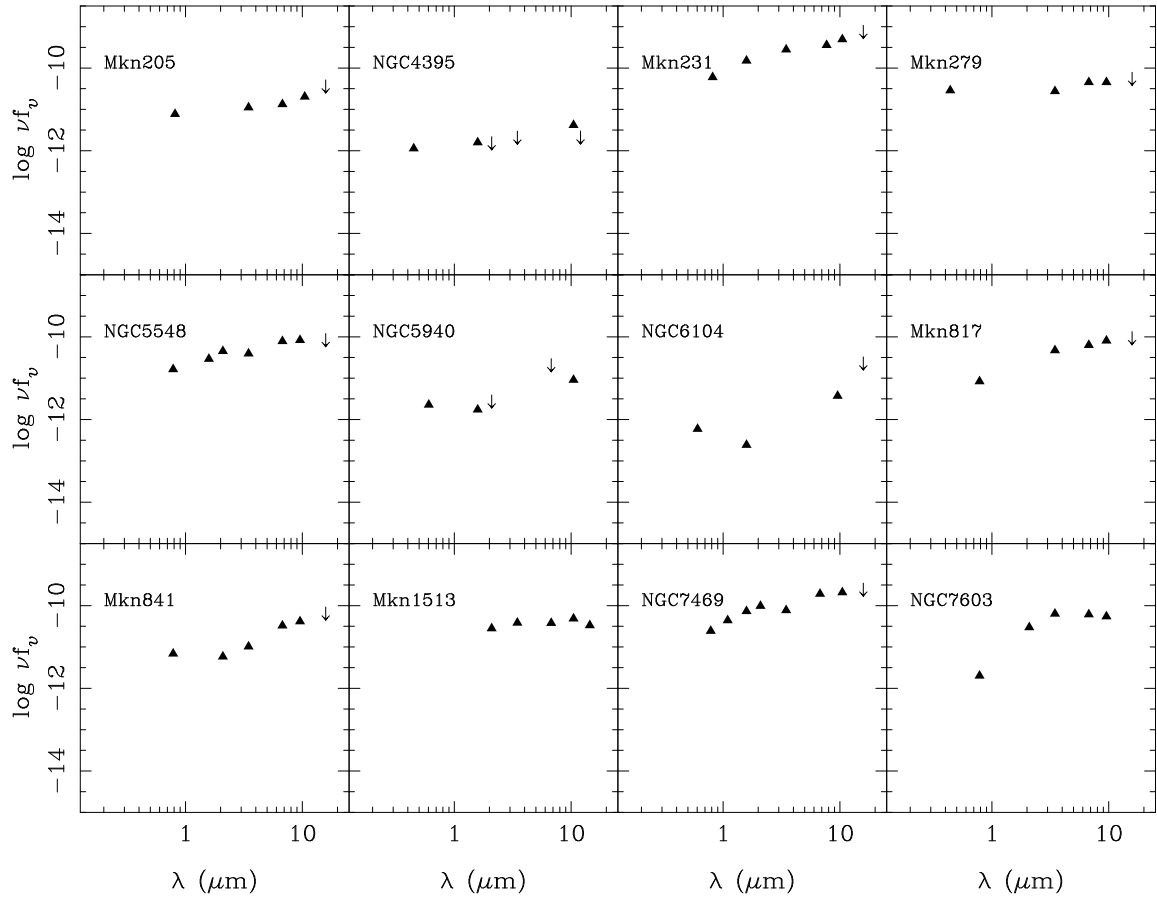


FIG. 3B.— Continued.

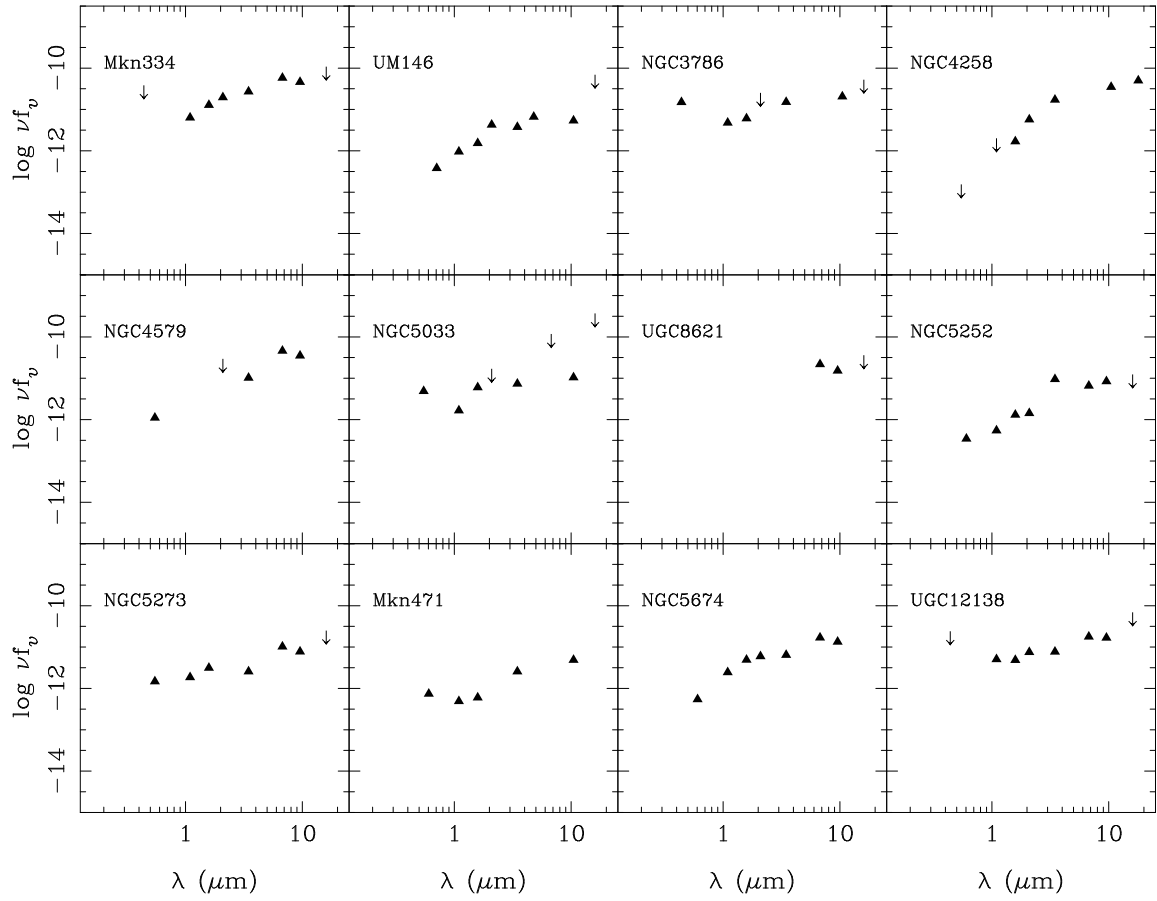


FIG. 4A.— Observed non-stellar SEDs (νf_ν) of optically classified intermediate type (1.8 – 1.9) CfA Seyferts in units of $\text{erg cm}^{-2} \text{s}^{-1}$.

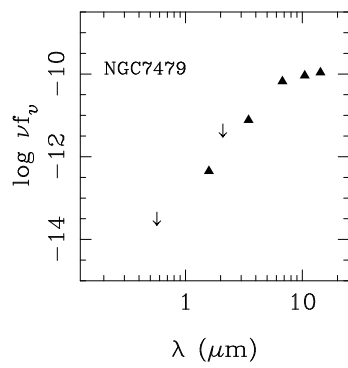


FIG. 4B.— Continued.

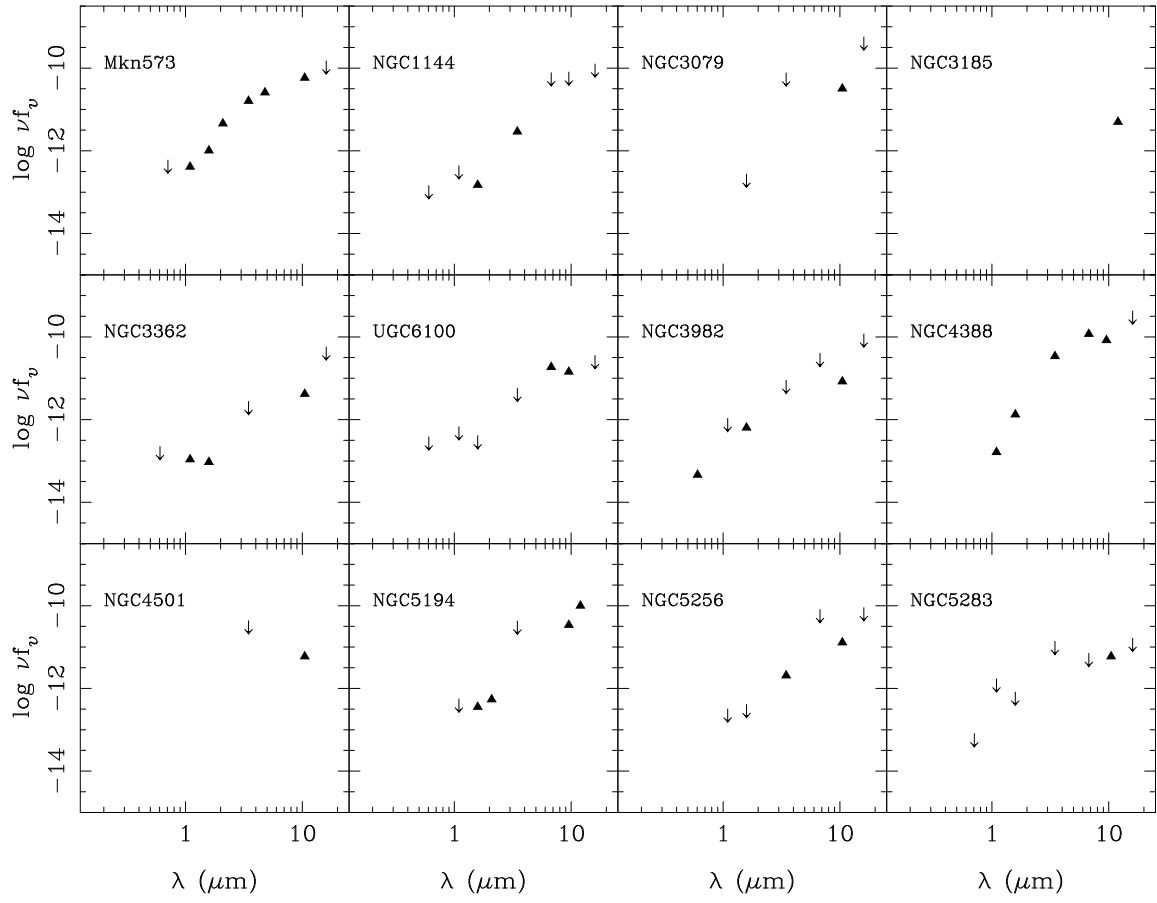


FIG. 5A.— Observed non-stellar SEDs (νf_ν) of optically classified type 2 CfA Seyferts in units of $\text{erg cm}^{-2} \text{s}^{-1}$.

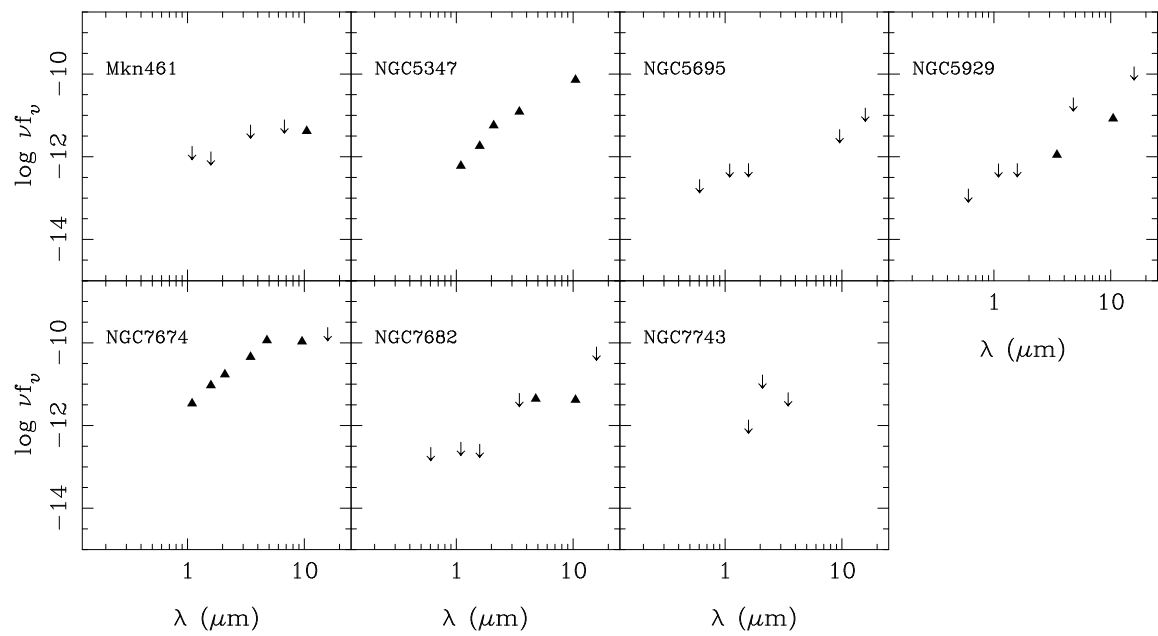


FIG. 5B.— Continued.

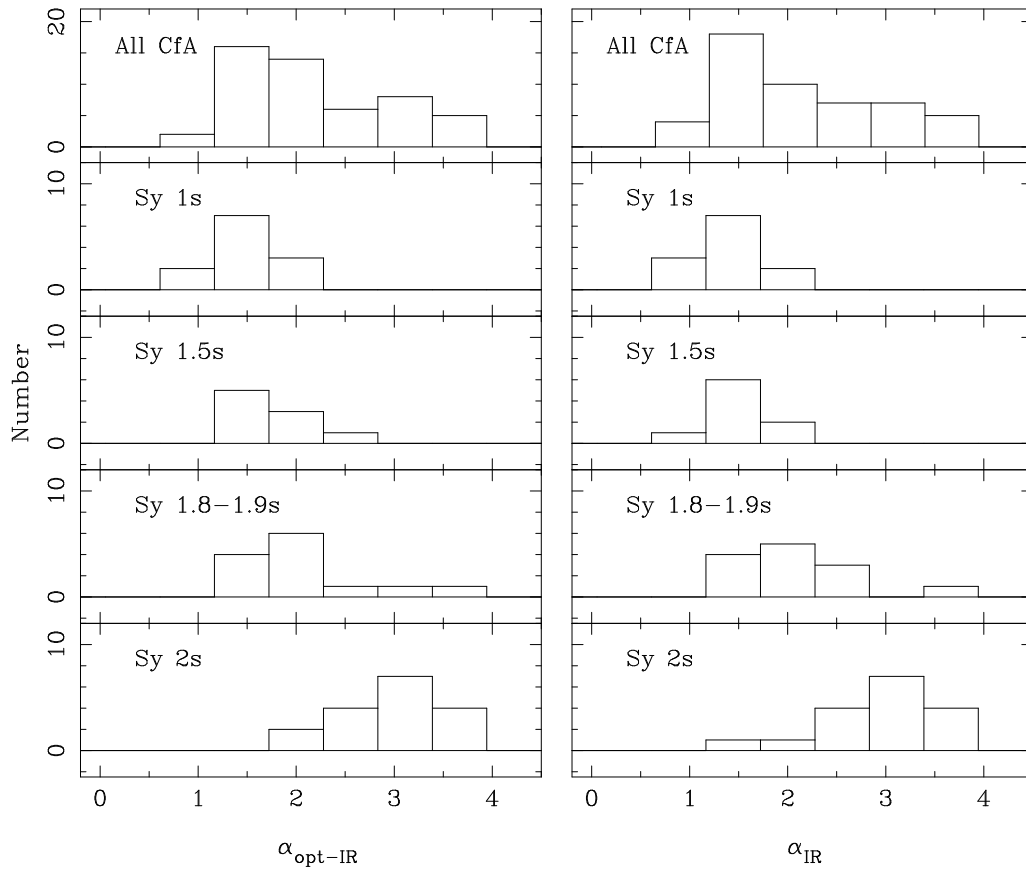


FIG. 6.— Distributions of the fitted spectral indices ($f_\nu \propto \nu^{-\alpha}$) in the optical-infrared wavelengths ($\alpha_{\text{opt-IR}}$ for the spectral range $\simeq 0.4 - 16 \mu\text{m}$, left panels) and infrared wavelengths (α_{IR} for the spectral range $1 - 16 \mu\text{m}$, right panels). The very top panels are the 51 Seyferts in the 'extended' CfA sample with measured spectral indices. The panels below are the same sample broken up in different Seyfert types as derived from optical spectroscopy.

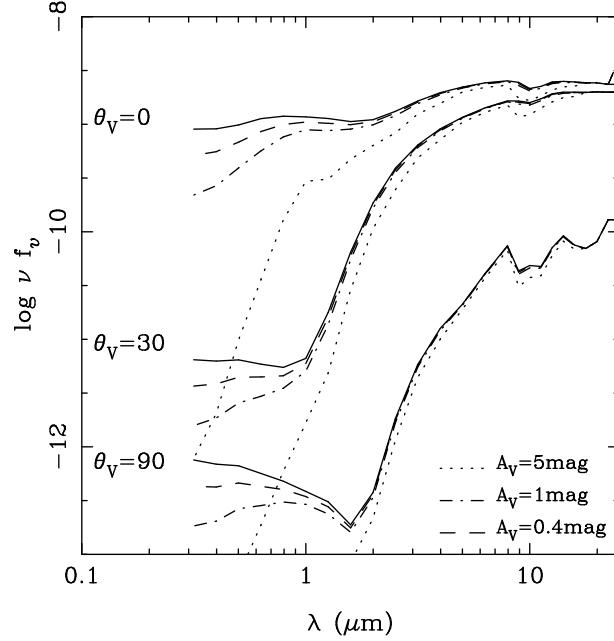


FIG. 7.— Effects of foreground extinction ($A_V = 0.4, 1$ and 5 mag) on the observed SED of an AGN, using Rieke & Lebofsky (1985) extinction law. The AGN SEDs are outputs of the Torus+Cone model from Efstathiou & Rowan-Robinson 1995 (see Section 6 and Table 8 for details) for three different viewing angles. $\theta_v = 0^\circ$ is the polar view of the AGN, $\theta_v = 30^\circ$ is an intermediate view (corresponding to the half opening angle of the torus, Θ_c), and $\theta_v = 90^\circ$ is the equatorial view (through the torus).

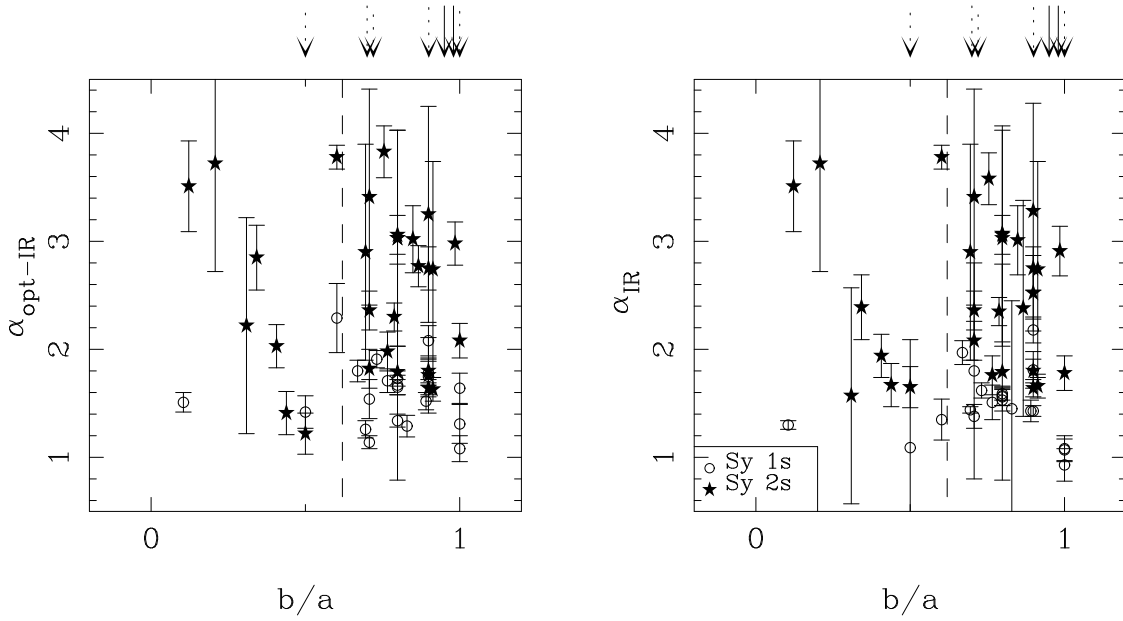


FIG. 8.— Fitted optical-infrared (left panel) and infrared (right panel) spectral indices (see Section 5) as a function of the inclination of the host galaxy, where $b/a = 0$ is an edge-on galaxy, and $b/a = 1$ is a face-on galaxy. The arrows at the top of the plots indicate the values of b/a for the remaining 7 galaxies with no measured spectral indices —dotted lines for the type 2s (green in the on-line version) and solid lines for the type 1s (red in the on-line version). The dashed line indicates a host galaxy axial ratio of $b/a = 0.6$ or an inclination of $i > 53^\circ$ (see discussion in text). The galaxies are separated between Seyfert 1s ($1 - 1.5$) shown as open circles (red in the on-line version) and Seyfert 2s ($1.8 - 2$) shown as filled star symbols (green in the on-line version), using the classification from optical spectroscopy.

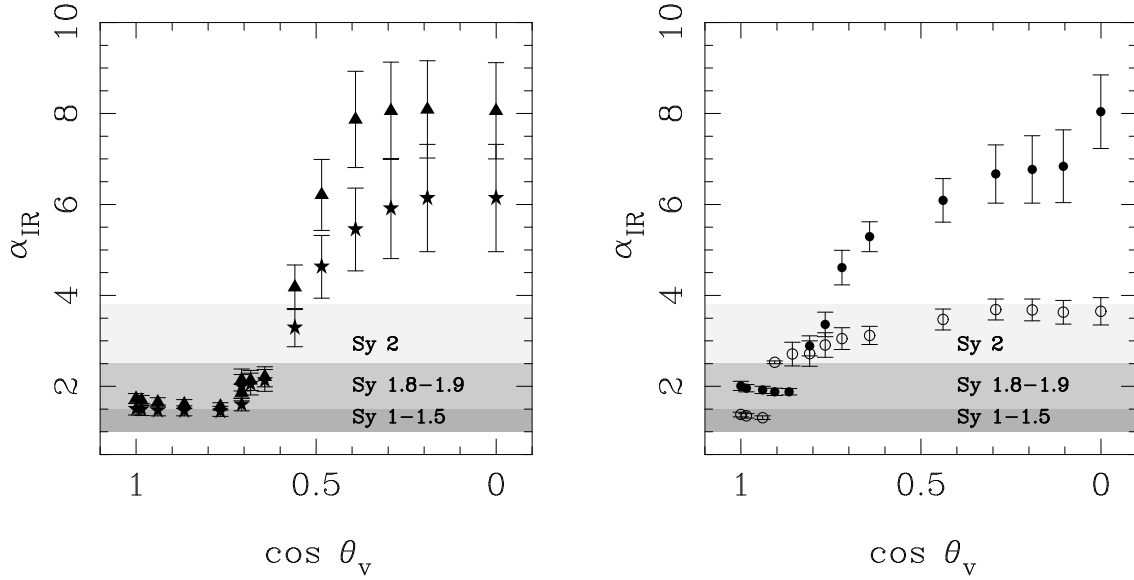


FIG. 9.— Predicted infrared spectral indices ($f_\nu \propto \nu^{-\alpha_{\text{IR}}}$) in the $1 - 16 \mu\text{m}$ spectral range as a function of the cosine of the viewing angle to the torus ($\theta_v = 0^\circ$ polar view of the AGN, $\theta_v = 90^\circ$ equatorial view of the AGN) using Efstathiou & Rowan-Robinson (1995) and Efstathiou et al. (1995) torus models. *Left panel:* results for models with a torus half opening angle $\Theta_c = 45^\circ$, and two different equatorial UV optical depths: $\tau_{\text{UV}} = 500$ mag (filled triangles), $\tau_{\text{UV}} = 250$ mag (filled stars), Models Torus 2 and Torus 3 respectively (see Table 8). *Right panel:* results for a torus model with a half opening angle $\Theta_c = 30^\circ$, and an equatorial UV optical depth of $\tau_{\text{UV}} = 1200$ mag with the cone component (Model Torus+Cone in Table 8, open circles) and without the cone component (Model Torus 4 in Table 8, filled circles). In both diagrams the shaded areas represent the observed ranges of fitted α_{IR} for Seyfert 1 – 1.5s (darkest shaded area), Seyferts 1.8 – 1.9s (intermediate shaded area), and Seyfert 2s (lightest shaded area) in the CfA sample.